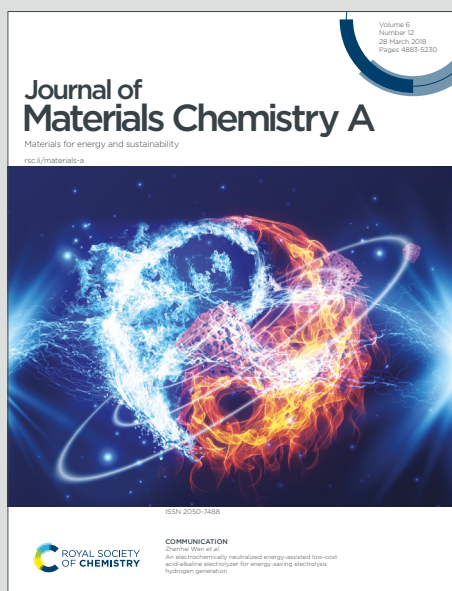


Journal of Materials Chemistry A

Materials for energy and sustainability

Accepted Manuscript

This article can be cited before page numbers have been issued, to do this please use: A. López-García, A. J. Carrillo del Teso, C. Jiménez, R. Suarez Anzorena, R. Garcia-Diez, V. Pérez-Dieste, I. J. Villar-García, A. B. Hungría, M. Bär and J. M. Serra, *J. Mater. Chem. A*, 2024, DOI: 10.1039/D4TA03146F.



This is an Accepted Manuscript, which has been through the Royal Society of Chemistry peer review process and has been accepted for publication.

Accepted Manuscripts are published online shortly after acceptance, before technical editing, formatting and proof reading. Using this free service, authors can make their results available to the community, in citable form, before we publish the edited article. We will replace this Accepted Manuscript with the edited and formatted Advance Article as soon as it is available.

You can find more information about Accepted Manuscripts in the [Information for Authors](#).

Please note that technical editing may introduce minor changes to the text and/or graphics, which may alter content. The journal's standard [Terms & Conditions](#) and the [Ethical guidelines](#) still apply. In no event shall the Royal Society of Chemistry be held responsible for any errors or omissions in this Accepted Manuscript or any consequences arising from the use of any information it contains.

Understanding the evolution of ternary alloyed nanoparticles during reversible exsolution from double perovskite oxides

View Article Online

DOI: 10.1039/D4TA03146F

Andrés López-García¹, Alfonso J. Carrillo^{1*}, Catalina E. Jiménez², Rosario Suarez Anzorena^{2,3}, Raul Garcia-Diez², Virginia Pérez-Dieste⁴, Ignacio J. Villar-Garcia^{4,5}, Ana B. Hungría⁶, Marcus Bär^{2,7,8}, José M. Serra^{1*}

¹*Instituto de Tecnología Química, (Universitat Politècnica de València-Consejo Superior de Investigaciones Científicas), Valencia, Spain*

²*Dept. Interface Design, Helmholtz-Zentrum Berlin für Materialien und Energie GmbH (HZB), Albert-Einstein-Str.15, 12489, Berlin, Germany*

³*Unidad de Investigación y Desarrollo Estratégico para la Defensa (UNIDEF-CONICET-MINDEF), CITEDEF, J.B. de La Salle 4397, Buenos Aires, Argentina*

⁴*ALBA Synchrotron, Carrer de la Llum 2-26, 08290 Barcelona, Spain.*

⁵*Universidad CEU San Pablo, Facultad de Farmacia, Departamento de Química, Urbanización Montepríncipe, 28668 Boadilla del Monte, Madrid, Spain.*

⁶*Departamento de Ciencia de Materiales, Ingeniería Metalúrgica y Química Inorgánica, Universidad de Cádiz, Campus Río San Pedro, 11510 Puerto Real, Spain.*

⁷*Dept. X-ray Spectroscopy at Interfaces of Thin Films, Helmholtz-Institute Erlangen-Nürnberg for Renewable Energy (HI ERN), Albert-Einstein-Str. 15, 12489 Berlin, Germany*

⁸*Department of Chemistry and Pharmacy, Friedrich-Alexander-Universität Erlangen-Nürnberg (FAU), Egerlandstr. 3, 91058 Erlangen, Germany*

Corresponding authors: jmserra@itq.upv.es alcardel@itq.upv.es



Abstract

View Article Online
DOI: 10.1039/D4TA03146F

Multicomponent nanoparticle exsolution has emerged as a promising process for obtaining highly active catalysts supported on perovskite oxides. For instance, FeCoNi alloys can be exsolved from $\text{Sr}_2\text{FeCo}_{0.2}\text{Ni}_{0.2}\text{Mn}_{0.1}\text{Mo}_{0.5}\text{O}_{6-\delta}$, boosting the electrocatalytic properties of these electrodes. However, due to differences in cation diffusion properties, the composition of the nanoparticles is uneven and strongly affected by process conditions such as temperature. An additional key feature of exsolution is its reversibility, which could help in catalyst regeneration if poisoned. Nevertheless, there is little knowledge on the reversibility mechanisms of multicomponent exsolved alloys. For that purpose, a combination of synchrotron-based in-situ X-Ray Diffraction (XRD) and Near-Ambient Pressure X-Ray Photoelectron Spectroscopy (NAP-XPS) was employed in this work to uncover these missing aspects of multicomponent alloyed exsolution. These techniques allowed determining the crystallographic and surface-related phenomena occurring during reversible exsolution both to the nanoparticles and the perovskite oxide support. This enabled the identification of the exsolution onset temperature and the range at which the double perovskite to Ruddlesden-Popper transition occurred, a process that has notable implications for the electrocatalytic performance. Finally, in combination with microscopy analyses, it was possible to reveal the morphological and compositional changes that the exsolved nanoparticles experienced upon reduction-oxidation cycles. This resulted in a re-arrangement of the surface species and a variation in the composition (Fe enrichment) of the regenerated ternary alloyed exsolved nanoparticles. These results indicate that reversible exsolution might alter the catalytic properties of the exsolved nanoparticles, with profound implications in the performance of (electro)catalytic processes.



1. Introduction

Nanoparticle (NP) exsolution has emerged in the last decade as a promising metallic nanocatalyst fabrication route¹⁻³. It has been mainly applied to develop electrocatalysts for solid oxide fuel cells and electrolyzers, although, in the last years, its range of application has been extended to other energy-relevant processes⁴, such as syngas production via methane reforming⁵⁻⁸ or chemical looping⁹⁻¹³, CO₂ hydrogenation¹⁴, or even as gas sensors^{15,16} and resistive switches¹⁷. Exsolution consists of the migration of metal transition cations that, under reducing conditions, diffuse to the surface, where they nucleate as metallic NPs. Since the particles emerge from the bulk, they remain anchored or socketed to the oxide surface, conferring high stability and robustness versus catalytic degradation phenomena such as high-temperature sintering or coking¹⁸. In addition, exsolution offers high versatility in terms of morphological and compositional NPs tuning, which can be easily adjusted by controlling the external (processing) or intrinsic (material design) parameters¹⁹. For instance, higher temperatures and longer exposure times lead to larger particles and decrease the NP dispersion^{17,20}. Additionally, the NP shape can be modified by changing these parameters⁸ or the type of reducing gas (CO instead of H₂)²¹. Regarding intrinsic parameters tunability, by carefully choosing the perovskite B-site cations, it is possible to obtain multi-element alloyed NPs²². This has led to the evolution of bimetallic alloys such as FeNi²³⁻³¹ CoFe³²⁻³⁴, or even ternary alloyed FeCoNi NPs^{6,35,36}. Ternary alloy exsolution is less explored than bimetallic exsolution, although it shows high promise in terms of catalytic activity. For instance, Joo et al. reported that exsolved alloyed FeCoNi NPs presented higher CH₄ conversion in dry reforming reactions compared to metallic Ni and CoNi bimetallic NPs. This improvement was ascribed to an upshift of the d-band center, which helped in the charge donation and caused a weakening of the reactants bond strengths⁶. However, very few works have been devoted to a better understanding of ternary alloyed NP exsolution. In a previous work, FeCoNi alloyed NPs were exsolved from Sr₂FeCo_{0.2}Ni_{0.2}Mn_{0.1}Mo_{0.5}O_{6-δ}²⁰. This double perovskite material family has shown promising electrochemical properties for CO₂ electrolysis, especially when combined with NP exsolution^{29,34,37,38}. Interestingly, by varying the exsolution temperature, NP composition, size and dispersion can be modulated. For instance, by performing the exsolution at 800 °C, the amount of Fe in the NPs is almost twice that of the exsolution at 600 °C. At these temperatures, Ni is always the element in highest concentration²⁰. These results showed that, by carefully controlling



the exsolution processing conditions, the composition of the NPs can be tuned, which might have profound effects on reaction conversion and/or selectivity in multiple chemical processes. However, there is still little understanding of the underlying mechanism of ternary alloy exsolution and the migration/growth kinetics of the different cations involved. For that reason, in this work, we have studied ternary alloy exsolution from double perovskites using synchrotron-based in-situ Near-Ambient Pressure X-Ray Photoelectron Spectroscopy (NAP-XPS) and X-Ray Diffraction (XRD) to shed light on both the surface properties and crystallographic evolution during exsolution. Furthermore, we have, in-situ, assessed the reversibility of the exsolution process by performing reduction-oxidation cycles to gain valuable information about the regeneration of the exsolved NPs. Exsolution reversibility, also called self-regeneration, was one of the first key advantages that this process exhibited, already identified in the first reports on exsolution in literature^{39–42}. However, there is scarce understanding on how self-regeneration occurs during the exsolution of ternary alloys, concerning the nature and morphology of the NPs associated with the perovskite surface restructuring and crystallographic stability. Hence, in this work, we also deepen our understanding of ternary alloyed exsolved NP regeneration by considering all these aspects.

2. Experimental methods

2.1. Materials fabrication

Double perovskites were fabricated following the protocol described in a previous work²⁰. Briefly, powders of $\text{Sr}_2\text{FeCo}_{0.2}\text{Ni}_{0.2}\text{Mn}_{0.1}\text{Mo}_{0.5}\text{O}_{6-\delta}$ were synthesized by a modified Pechini method. Metal precursors, $\text{Sr}(\text{NO}_3)_2$ (99%, Aldrich), $\text{Fe}(\text{NO}_3)_3 \cdot 9\text{H}_2\text{O}$ (98%, Aldrich), $\text{Co}(\text{NO}_3)_2 \cdot 6\text{H}_2\text{O}$ (99%, Aldrich), $\text{Ni}(\text{NO}_3)_2 \cdot 6\text{H}_2\text{O}$ (98.5%, Aldrich), $\text{Mn}(\text{NO}_3)_2 \cdot 4\text{H}_2\text{O}$ (98%, Aldrich) and $\text{H}_{24}\text{Mo}_7\text{O}_{24}\text{N}_6 \cdot 4\text{H}_2\text{O}$ (99%, Aldrich) were dissolved in distilled water, together with citric acid (CA, 99%, Alfa Aesar) using a molar ratio metal precursor:CA of 1:1.5, under constant stirring at 60 °C. Once dissolution was completed, ethylene glycol (EG, 99%, Aldrich-Merck) was added as a complexing agent (CA:EG ratio of 2/3 wt. %) and the temperature was raised to 80 °C for faster water elimination for 2 hours. After most of the water was evaporated, the solution was transferred to a drying oven and heated to 220 °C overnight for gelification, followed by the calcination of the formed gel. The solid obtained was grounded in agate mortar to fine powders, then sintered at 1100 °C in air for 12 hours. Ex-situ exsolution treatments were



carried out in a horizontal tubular furnace under 5% H₂/Ar flow and at the temperature conditions detailed in the following sections.

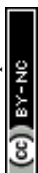
View Article Online
DOI: 10.1039/D4TA03146F

2.2. Morphological characterization

High-Resolution Field Emission Scanning Electron Microscopy (HRFESEM) characterization was done with a GeminiSEM 500 from Zeiss. High-Resolution Scanning Transmission Electron Microscopy, HRSTEM, analyses were performed at 200 kV on a double aberration-corrected FEI Titan3 Themis 60-300 microscope. The instrument is equipped with a monochromatic, high-brightness XFEG source and a high-sensitivity Super-X-EDS system composed of 4 window-less SDD detectors symmetrically arranged around the sample and the objective lens pole pieces. The Energy Dispersive X-ray Spectroscopy (XEDS) maps were acquired using a beam current of 50 pA, convergence angle of 19 mrad and 20 keV. Oxidized and re-exsolved NPs were analyzed with a JEM 2100F at 200 kV. Also, XEDS was performed to study compositions of exsolved NPs with an XEDS X-Max 80 Oxford Instruments.

2.3. In-situ X-ray Diffraction

In-situ X-ray diffraction (XRD) was performed at the BL04-MSPD beamline located at the ALBA synchrotron. Pristine (fine powder) samples were placed in the central zone of quartz capillaries of 1/8 inch outer diameter. The capillaries were connected to the gas delivery system, which consisted of a set of mass flow controllers delivering either 5% H₂/Ar or synthetic air. The samples were heated with a FMB Oxford hot air blower (see **Figure S1b** for more details). A PSD Mythen detector was used, using a wavelength of 0.41345 Å. Scans covered a 2θ range of 0-35°. In a typical run (see **Figure S3**), in-situ XRD was performed while heating up to the desired temperature in 5% H₂/Ar. Then, after an isothermal period of 4 h in the same reducing conditions, the gas was switched to synthetic air for 2 h. Finally, a second reducing isothermal treatment of 2 h was performed by changing back to 5% H₂/Ar to check the exsolution regeneration. Exsolution reversibility was evaluated at two different temperatures, 600 and 800 °C. It should be noted that the exsolutions were performed under dry conditions in order to replicate our previous work²⁰, thus, the effect pO₂ might suffer variations over the course of the experiment. This could be fixed by performing the exsolutions with controlled pH₂O, however, it should be kept in mind that working under humidified conditions could also affect the exsolution process by itself.



2.4. In-situ Near Ambient Pressure XPS

View Article Online
DOI: 10.1039/D4TA03146F

Near Ambient Pressure X-ray Photoelectron Spectroscopy (NAP-XPS) was performed at the BL-24 CIRCE beamline located at the ALBA synchrotron⁴³. This beamline provides an energy resolution of $E/\Delta E \sim 8000$. Porous pellets of the perovskite oxide were held by a 0.12 mm thick Pt foil onto the sample holder. An IR laser (up to 150 W power) was used for sample heating (**Figure S1a**). The in-situ NAP-XPS measurements were performed in several stages. First, a cleaning step was performed by heating the sample up to 600 °C in a pure O₂ atmosphere (0.2 mbar) to remove carbonaceous species from the surface. At this point, NAP-XPS was performed to record data in the pristine state. After the cleaning period, the temperature was lowered to 300 °C, from where the sample was slowly heated up to 600 °C in a pure H₂ atmosphere (0.2 mbar). The formation of metallic species was first monitored by following changes in the valence band (VB) and in the Ni 2p_{3/2} core level spectrum. Once the VB showed changes indicative of a metallic phase (i.e., appearance of spectral intensity at the Fermi edge at 0 eV binding energy, BE), Ni 2p_{3/2}, Co 2p_{3/2}, and Fe 2p_{3/2} core level spectra were measured in intervals of 25 °C until reaching ~600 °C (max. temperature allowed by the set-up). After reaching this temperature, a complete survey spectrum of all the elements contained in the perovskite was collected. Finally, the gas atmosphere was switched back to pure O₂ (0.2 mbar) to analyze the reversibility of the exsolution process. For the pristine, reduced and re-oxidized states, several sample depths were analyzed by tuning the photon energy such that the photoemission lines of interest were collected at different kinetic energies. Mo 3d, O 1s, and Sr 3d spectra were fitted with CasaXPS, using a Shirley background and a Gaussian-Lorentzian (30) line shape. The thick Pt foil that held the pellet was used for energy calibration, setting the Pt 4f_{7/2} to a BE of 71.1 eV.

3. Results

3.1. Ternary alloyed nanoparticle exsolution formation

3.1.1. Crystallographic evolution probed with in-situ XRD under reducing conditions.

In this first section, the exsolution of the ternary-alloyed NPs will be assessed under a temperature-programmed reduction scheme, both using in-situ NAP-XPS and XRD. **Figure S2a** depicts the X-ray diffractogram pattern of the Sr₂FeCo_{0.2}Ni_{0.2}Mn_{0.1}Mo_{0.5}O_{6-δ} sample before exsolution. The XRD matches with the expected cubic phase (space group



$Fm\bar{3}m$). A very minor presence of NiO impurities were detected, which was not inferred in our previous work when using lab-based XRD²⁰. Despite this, it was possible to in-situ monitor the decomposition of NiO, benefitting from the high-resolution synchrotron-based equipment. During this first set of experiments, the $Sr_2FeCo_{0.2}Ni_{0.2}Mn_{0.1}Mo_{0.5}O_{6-\delta}$ sample powders (contained in capillaries) were subjected to a heating stage up to 820 °C under a constant flow of 5% H₂/Ar atmosphere while in-situ monitoring changes occurring during the reduction process via XRD. Here, we will focus on two main diffraction regions. First, the one around 8.52 ° ($\lambda = 0.41345 \text{ \AA}$), which corresponds to the double perovskite's (2 2 0) main reflection. Secondly, the region around 11.4-11.6 °, where the reflections ascribed to the main signals of metallic phases are expected to appear. Therefore, a double objective is pursued: to evaluate the possible perovskite transformation under high-temperature reduction conditions and explore the formation of the multi-metallic exsolved NPs.

Figure 1a shows the changes affecting the (2 2 0) reflection of the double perovskite under constant heating in a 5% H₂/Ar atmosphere in the 400-820 °C region. Upon heating, a shift to lower 2θ values can be observed, which is ascribed to a lattice expansion of the double perovskite phase. During the reduction treatment that leads to the exsolution process, H₂ reacts with the perovskite lattice oxygen, creating oxygen vacancies in the perovskite. In addition, reducible cations in the bulk phase will lower its oxidation state, increasing their ionic radii. These two chemical processes cause the lattice expansion. During this initial heating stage, only a very minor emergence of a Ruddlesden-Popper (RP) phase was inferred (Sr_3FeMoO_7 , I4/mmm tetragonal structure). This can be observed in **Figure 1c**, where a minor contribution of an RP phase at around 8.31 ° appears at temperatures above 780 °C. In our previous work, we confirmed the formation of this RP phase and identified it as one of the reasons for the lower performance of the electrodes exsolved at 800 °C versus the electrodes exsolved at 600 °C, since the former exhibited a higher tendency to form SrCO₃ species under CO₂ electrolysis conditions²⁰.

Figure 1b shows the crystallographic changes occurring in the 11.2-11.6 ° region, in which metallic reflections are expected. Starting at 400 °C, the reflections associated with NiO impurities are observed at 11.3 °. During the temperature increase to 715 °C, this signal slightly shifts to lower 2θ values due to thermal lattice expansion. At this temperature, the NiO reflection vanishes, and a peak around 11.55 ° emerges, indicating the formation of a metallic phase. With increasing temperature further (715-820 °C



range), the signal broadens asymmetrically and the main peak shifts to 11.5° . For a clearer view, **Figure 1d** shows the transition in this temperature region (from 700 to 820 °C). The progressive disappearance of the NiO is expected to lead to the formation of metallic Ni, in agreement with our XRD data. The metallic Ni formation from NiO was already observed via HRFSEM in our previous works, where polygonal cavities around certain particles could be seen, typically formed after NiO reduction²⁰. This process slightly interferes with the detection of the exsolved metallic phase since Ni and the possibly forming ternary alloy FeCoNi would show diffraction peaks at almost identical 2θ angles. Unfortunately, there are few references for crystallographic information on FeCoNi, as it is $\text{Co}_{0.027}\text{Fe}_{0.283}\text{Ni}_{0.689}$, the closest composition to the expected exsolved ternary alloys. This composition ($Fm\bar{3}m$ space group) presents its most intense reflection at 11.58° (COD 9000088), whereas, for metallic Ni, it is around 11.59° (ICSD 250535, data at room temperature). Therefore, two distinct reflections might appear in a narrow 2θ range. This can be better observed in **Figure S2b**, which shows the 11.0 - 12.6° region, depicting the appearance of two distinct reflections: one at 11.60° (ascribed to Ni) and another at 11.54° , which suggests the formation of the exsolved metallic alloy. Here, it should be noted that ex-situ STEM-XEDS analyses performed after a reduction treatment at 800 °C for 4 h (**Figure 1e**) show the presence of ternary-alloyed NPs mainly composed of Ni and, to a lesser extent, Co and Fe²⁰. This might alter the positions at which the ternary alloy appears if compared to the database pattern, which slightly differs in composition. By increasing the temperature, the exsolved alloy peak shifts to 11.5° , whereas the Ni metallic peak remains almost unaltered at the same position (**Figure 1d**). This shift may, hence, be attributed to a change in the composition of the exsolved metal alloy. However, the influence of thermal expansion cannot be discarded. The formation of Ni-rich nuclei may occur in the early stages of the exsolution process, facilitating the incorporation of either Co and/or Fe afterwards. This shall be especially considered for the case of Fe since in this family of Sr-Fe-Mo-based perovskites, Fe exsolution has been scarcely reported and usually requires a more reducible cation (for instance, Ni or Co) to allow the formation of Fe-based bimetallic alloys. This was observed in Carrillo and Serra's work, in which a double perovskite with just Fe and Mo on the B-site does not lead to the creation of exsolved NPs, whereas a partial substitution with Ni leads to a remarkable bimetallic exsolution under the same conditions⁵. It is important to highlight that these Ni-rich nuclei come from the Ni exsolution, and not from the Ni^0 produced due to the reduction of NiO impurities. This fact lies on our previous studies with these materials,



where the presence of NiO impurities acted detrimentally to the nucleation during exsolution. A-site deficient materials exhibited lower NP populations with increasing NiO amounts. Therefore, we could rule out that the Ni⁰ coming from NiO reduction is acting as preferential nucleation sites²⁰.

Another exciting feature is observed when comparing **Figure 1a** and **1b**. The formation of the exsolved metallic particles occurs at the same temperature (between 715 and 720 °C) at which an inflection is observed in the double perovskite main reflection, together with a peak narrowing (**Figure 1a**). This might be a combination of crystal cell expansion caused by the reduction of the lattice cations during the exsolution process and peak narrowing due to the disappearance of some secondary phase at around 8.5 ° (**Figure 1c**, 358 °C diffractogram) that causes an asymmetrical peak shape. In addition, the asymmetrical peak broadening visible at temperatures above 760 °C (**Figure 1b**) is ascribed to the appearance of the (0 0 10) reflection of the RP phase previously mentioned. For a better view of the evolution affecting the crystal phases during the heating, diffractograms including the whole measured 2θ range are depicted in **Figure S2c**.

View Article Online
DOI: 10.1039/D4TA03146F



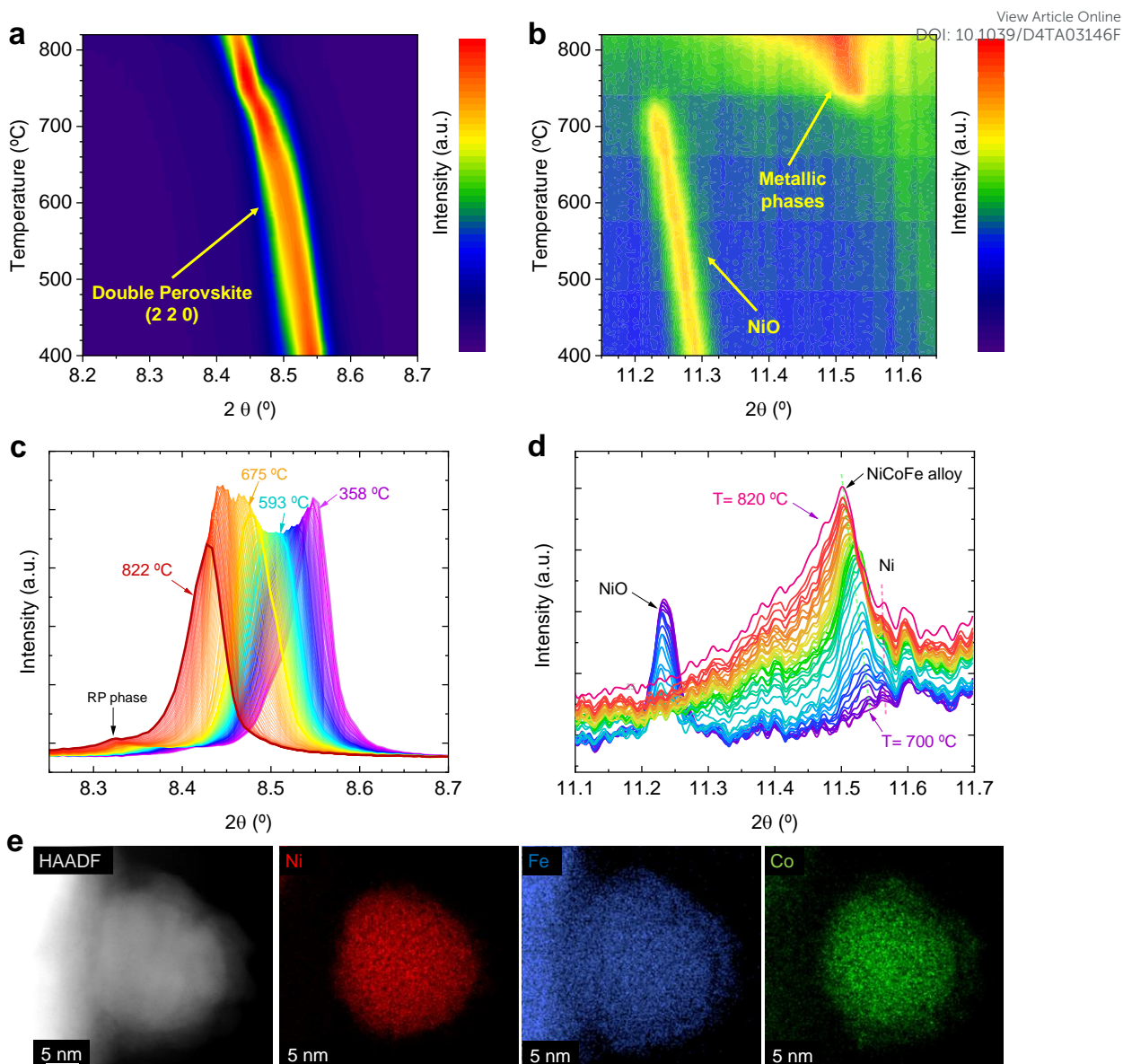


Figure 1. Contour maps depicting the X-ray diffraction changes occurring in the (a) 8.2-8.7° and (b) 11.1-11.7° 2θ regions, respectively, when heating up the $\text{Sr}_2\text{FeCo}_{0.2}\text{Ni}_{0.2}\text{Mn}_{0.1}\text{Mo}_{0.5}\text{O}_{6-\delta}$ sample up to 800 °C, under 5% H_2/Ar flow. X-ray diffractograms of the (c) 8.2-8.7° and (d) 11.1-11.7° 2θ regions depicting the changes in the main perovskite reflection and the metallic phases, respectively. (e) High-Angle Annular Dark-Field from Scanning Transmission Electron Microscope (HAADF-STEM) image and XEDS maps of a ternary alloyed exsolved NP with a cationic ratio $\text{Co}_{0.28}\text{Fe}_{0.18}\text{Ni}_{0.54}$ from $\text{Sr}_2\text{FeCo}_{0.2}\text{Ni}_{0.2}\text{Mn}_{0.1}\text{Mo}_{0.5}\text{O}_{6-\delta}$. These images were taken ex-situ after a treatment of 4 hours exsolution at 800 °C in a 5% H_2/Ar atmosphere.

3.1.2. Surface property evolution upon in-situ heating in reducing conditions monitored by NAP-XPS

Next, the focus will be on the evolution of surface chemistry during heating under reducing conditions using NAP-XPS. Here, the measuring conditions differ from the in-situ XRD experiments since reduction was performed at 0.2 mbar under pure H_2 . These



conditions might imply slight changes in the temperature at which NPs appear with respect to the ambient pressure experiments in 5% H₂/Ar used for XRD. **Figures 2a-c** show the Ni 2p_{3/2}, Co 2p_{3/2}, and Fe 2p_{3/2} core level spectra recorded at different temperatures under H₂ atmosphere. Note that the Fe 2s photoemission line is expected to have a BE 8 eV lower than that of the Ni 2p_{3/2} line and, hence, might contribute to the spectral background in that region. The spectra were acquired with a constant electron kinetic energy of 400 and 150 eV, corresponding to a photoelectron Inelastic Mean Free Path (IMFP)⁴⁴ of ca. 1.0 and 0.6 nm, respectively, calculated based on the NIST Standard Reference Database 71⁴⁵. The exponentially decaying sampling depth is estimated to be up to three times the IMFP^{46,47}, so we derive ca. 3.0 and 1.8 nm for 400 and 150 eV electron kinetic energy, respectively. However, 68 % of the photoelectrons stem from one IMFP of depth. Given the cubic lattice parameter of the pristine perovskite (0.78 nm²⁰), it is assumed that the XPS spectra acquired with 150 eV kinetic energy are more representative of the first outermost unit cell nearest to the solid/gas interface that we refer to as the “outer” surface layers. The spectra acquired with 400 eV kinetic energy probes slightly deeper in the solid, adding information on “subsurface” layers. It is also worth mentioning that the CIRCE beamline provides significantly higher photon flux at the excitation energies needed to acquire the Ni, Co and Fe 2p_{3/2} core level spectra with 400 than 150 eV photoelectron kinetic energy thus improving the time resolution for the spectra (**Figures 2 and 3**). Nevertheless, NAP-XPS is an ideal complement for understanding surface chemistry changes during exsolution treatment conditions. Here, the starting point was to track the changes in the valence band (VB) and the Ni 2p_{3/2} core level to discern when the metallic phases started forming. This could be inferred by the appearance of the Fermi edge in the VB region and the emergence of the spectral feature associated with metallic Ni or Fe in the Ni 2p_{3/2} or Fe 2p_{3/2} core-level region, respectively. Before the first measurements, the sample pellet was heated up under a CO₂-free oxygen atmosphere to the maximum temperature reachable with this set-up (600 °C) to remove possible carbonaceous species at the perovskite oxide surface. After this cleaning step, the sample was cooled to 300 °C, where the heating stage under reducing conditions started since no NP exsolution was expected at lower temperatures. The first Ni 2p_{3/2} core level spectra were collected at 350 °C, and the features indicate the presence of Ni²⁺ (854 eV), corresponding to Ni located in an oxide lattice. The spectra acquired at 475 °C showed the same features for Ni 2p_{3/2} (**Figure 2a**). At this temperature, Co 2p_{3/2} core level spectra were also acquired, **Figure 2c**, showing a main peak at a BE of 780.2 eV, which



could be ascribed to Co^{2+} in a perovskite oxide lattice⁴⁶. The first appearance of a metallic phase was detected at 525 °C for every exsolvable metal: Ni, Co, and Fe (**Figures 2a-c**). In the Ni $2p_{3/2}$ spectrum a peak emerged at 852.7 eV corresponding to Ni^0 , which increased in intensity with the reduction temperature. In parallel, the Ni^{2+} peak decreased in intensity and showed a shift of 1.0 eV to higher BE values (**Figure 2a**). This shift was related to a Fermi level shift within the perovskite band gap when changing from oxidizing to reductive atmospheres^{30,48}. In the case of the Co $2p_{3/2}$ core level spectra, the metallic peak emerged with lower intensity at 525 °C, as noticed by a small bump at around 778 eV. This Co^0 signal increased in intensity with increasing temperature, but more gradually than the Ni^0 contribution to the Ni $2p_{3/2}$ spectrum. Additionally, the peak at 780.3 eV, ascribed to Co^{2+} , did not significantly decrease its intensity when heating up to 600 °C. A similar case is observed for the Fe $2p_{3/2}$ core level spectra: Fe^0 is inferred at 525 °C (first spectra recorded for Fe) by a low-intensity signal appearing at 707 eV, whose intensity remained unaltered when increasing the temperature (**Figure 2c**). In the same figure, the peak at 710.7 eV, ascribed to oxide lattice Fe^{3+} , is predominantly Fe^{3+} with a contribution of Fe^{2+} . Although this distinction is hard to make, it can be appreciated in the characteristic satellite peaks in the complete Fe 2p region (**Figure 3c**). Likewise for Co and Ni (**Figure 3a-b**). In **Figure 2c**, the main peak of $\text{Fe}_{3/2}$ showed a slight intensity decrease and broadening, which implies the reduction of Fe^{3+} to Fe^{2+} followed by the appearance of Fe^0 metallic species during heating in reducing atmospheres. With all these results, the main conclusion from these temperature-resolved NAP-XPS measurements lies in the rate of metallic phase formation, which differs widely for each element. To reveal a kinetic trend, the metallic (Me^0) to oxidized (Me) phase ratio was quantified (Me^0/Me) at each temperature (**Figure 2d**). It is observed that the reduction of the oxidized species to the metallic phase occurs much faster for Ni than for Co and Fe. Namely, at ca. 600 °C, above 50% of the Ni in the near-surface termination is in a metallic phase, whereas for Co and Fe, it is around 7 and 3%, respectively. These results are consistent with our previous works, in which we reported that the ternary alloyed NPs are mainly formed by Ni, followed by Co and, lastly, Fe^{20} . The fact that Ni is more likely to exsolve has been previously described⁹, even computationally^{2,49}, but never explored with in-situ measurements of alloys before. The in-situ NAP-XPS derived faster migration kinetics of Ni during the exsolution process from oxidized to metallic phase, explaining its higher content in the NPs than found for Co or Fe. STEM-XEDS maps acquired after ex-situ exsolution at 600 °C (**Figure 2e**) confirmed the gradual depletion of Ni species



from the outer layers of the perovskite oxide, which explains a faster decrease of Ni^{2+} signal in the NAP-XPS measures with increasing temperature. At the same time, both Co and especially Fe, are present in a higher concentration in the host perovskite surface at this temperature.

View Article Online
DOI: 10.1039/D4TA03146F

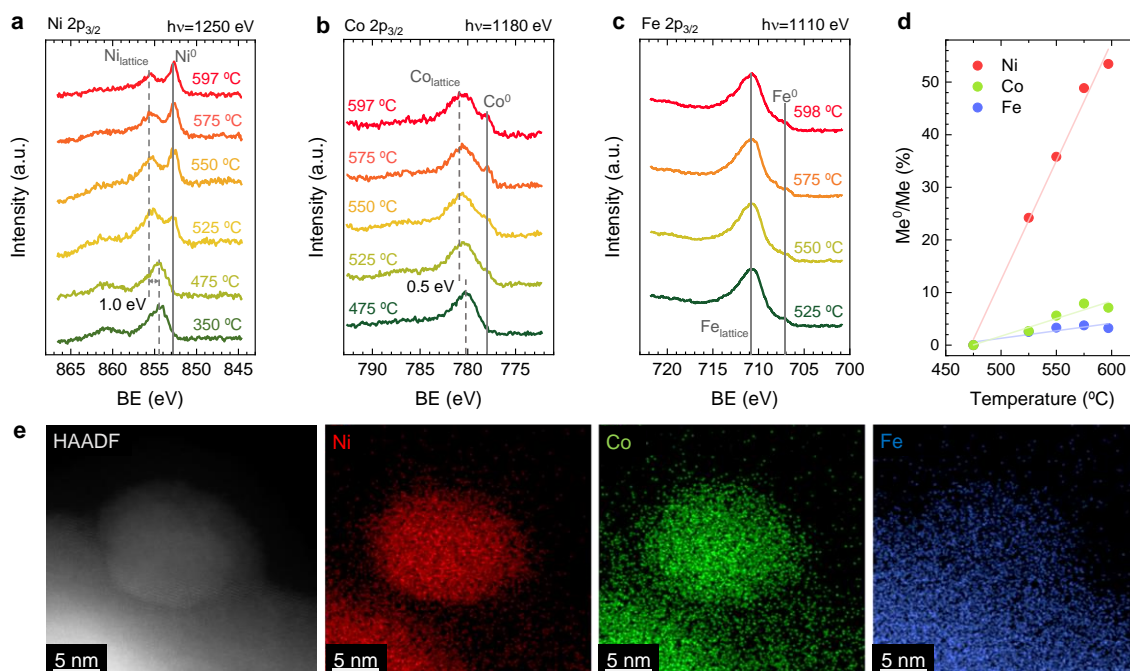



Figure 2. Evolution of NAP-XPS (a) Ni 2p_{3/2}, (b) Co 2p_{3/2}, and (c) Fe 2p_{3/2} spectra upon temperature-programmed reduction treatment. The used photon energies (to result in a similar electron kinetic energy of 400 eV) are indicated in the panels. A constant offset for better clarity is added to the spectra. (d) Variation of the metal to oxide content (Me⁰/Me) versus temperature for each element. (e) HAADF-STEM image and XEDS maps of a ternary alloyed exsolved NP with cationic ratio $\text{Co}_{0.28}\text{Fe}_{0.1}\text{Ni}_{0.63}$ from $\text{Sr}_2\text{FeCo}_{0.2}\text{Ni}_{0.2}\text{Mn}_{0.1}\text{Mo}_{0.5}\text{O}_{6-\delta}$. These images were taken ex-situ after a treatment of 4 hours exsolution at 600 °C in a 5% H_2/Ar atmosphere.

By combining the obtained results from both the in-situ XRD and NAP-XPS experiments, it is possible to unveil some mechanistic insights related to the exsolution of ternary alloys from $\text{Sr}_2\text{FeCo}_{0.2}\text{Ni}_{0.2}\text{Mn}_{0.1}\text{Mo}_{0.5}\text{O}_{6-\delta}$ double perovskites. First, from the in-situ XRD, we could rule out the formation of isolated monometallic exsolved NPs of Ni, Co, or Fe during exsolution in this system. This mechanism was introduced by Kwon et al. to explain the formation of CoNi alloys⁵⁰. Using in-situ XRD, the authors observed the formation of Co^0 and Ni^0 , which, upon heating, transformed into the metallic CoNi alloy. Additionally, DFT calculations performed by the authors established that the thermodynamically favored path consists of the co-segregation of isolated metallic cations and later aggregation on the surface, leading to the alloy formation. The less



Open Access Article. Published on 24 1446. Downloaded on 27/01/16 04:08:05 .
This article is licensed under a Creative Commons Attribution-NonCommercial 3.0 Unported Licence.



favored path might be the alloy formation in bulk followed by its exsolution. In this work, we observed the presence of metallic Ni, but resulting from the thermal reduction of NiO impurities. However, Fe and Co isolated metallic species were not detected even at high temperatures of 800 °C (**Figure 1**). In addition, no single-metal NP could be found during XEDS analyses, nor could it have a composition different from the explained FeCoNi alloy. Thus, the mechanism proposed by Kwon et al., even if thermodynamically more favorable than other scenarios, does not apply to our case. Alternatively, the case in which one of the exsolvable species acts as a nucleation site for the rest of the cations shall be considered. This hypothesis is based on the fact that, in this kind of double perovskites, exsolution has been scarcely observed from the undoped systems, e.g., Fe exsolution from $\text{Sr}_2\text{Fe}_{1.5}\text{Mo}_{0.5}\text{O}_{6-\delta}$ ⁵, and only when Ni and/or Co partially replaced Fe, it was possible to observe alloy exsolution^{29,34,51,52}. Lv et al. used in-situ STEM-XEDS for analyzing the formation of bimetallic CoFe alloys in $\text{La}_{0.4}\text{Sr}_{0.6}\text{Co}_{0.2}\text{Fe}_{0.7}\text{Mo}_{0.1}\text{O}_{3-\delta}$ ⁵³. They observed that, at 600 °C, the NPs were only formed by Co, whereas at 700 °C, the composition indicated FeCo alloy exsolution. Based on DFT results, Lv et al. argued that Fe exsolution is more energetically favored after Co vacancies formation. The authors' TEM analyses did not show the formation of isolated Fe NPs⁵³, which might also indicate a distinct mechanism than the one proposed by Kwon et al⁵⁰. It should be noted that both Kwon's and Lv's works studied different perovskite materials than analyzed in our work, which implies that differences in the materials properties, e.g., ionic diffusion, energy of vacancy formation (both for oxygen and cationic vacancies), foreseeably lead to variations in the exsolution mechanism. A good example is that isolated Fe exsolution has been reported in other perovskite systems, such as $\text{La}_{0.6}\text{Sr}_{0.4}\text{FeO}_3$ (LSF)⁵⁴⁻⁵⁶. Interestingly, in similar Co-doped ferrites, DFT calculations by Lv et al. showed segregation energies for Co and Fe in similar value ranges, around 0.5 eV. However, incorporation of Mo in the B-site increased these values to 0.7 and 1.79 eV, respectively⁵³. This result suggested a detrimental effect of Mo presence in Fe exsolution. In the same work, the authors also found that the formation of Co vacancies led to a decrease in the Fe segregation energy from 1.79 to 0.97 eV, revealing the importance of cationic vacancies in facilitating Fe exsolution. The same effect was also found by Lv et al. for $\text{Sr}_2\text{Fe}_{1.4}\text{Ru}_{0.1}\text{Mo}_{0.5}\text{O}_{6-\delta}$. In this system, DFT calculations resulted in a Fe segregation energy of 0.97 eV, which decreased to 0.65 and 0.37 eV when considering the presence of oxygen vacancies and Ru exsolution, respectively⁵⁷. Therefore, in this particular case, and based on the faster migration kinetics and exsolution behavior observed for Ni (**Figure 2d**), it might be

facilitating the exsolution of the other two metallic species (Co, Fe) acting as nucleation preferential sites and/or decreasing the segregation energies of Co and/or Fe. In addition, this fact also confirms that none of the hypotheses of Kwon et al. entirely satisfies the observed phenomena here.

3.2. Understanding exsolution redox reversibility

3.2.1 Changes in the surface chemistry upon reduction/oxidation cycles

After assessing the possible mechanism of ternary alloyed NP exsolution, in-situ synchrotron experiments focused on the redox capacity of these perovskites, including the exsolution reversibility. For that purpose, the surface chemistry evolution under reducing and oxidizing atmospheres was first investigated via in-situ NAP-XPS (**Figure S3**). **Figure 3** depicts a comparison of the evolution of Ni 2p, Co 2p, and Fe 2p core level spectra, acquired in-situ at 600 °C in pristine (0.2 mbar O₂), reduced (0.2 mbar H₂) and re-oxidized (0.2 mbar O₂) conditions. After reduction, and as expected seeing the previously exposed results, the three elements showed the appearance of their metallic phase, being more noteworthy for Ni, thus corroborating its higher concentration in the exsolved NPs. Ni²⁺ was also inferred, although when applying lower kinetic energy (150 eV, IMFP of 0.6 nm, **Figure S4**), this feature disappeared, indicating that, in the outer-surface layer, there is a depletion of oxidized Ni species, which is consistent with the STEM-XEDS ex-situ analyses (**Figure 2d**). In this outer-surface layer (**Figure S4**), the intensities of both metallic Co and Fe were also higher than when performing the measurements with a constant electron kinetic energy of 400 eV. After reoxidation, the metallic peaks of the three elements disappeared, resulting in spectra almost identical to the pristine state (**Figure 3a-c**). This is the first indication of ternary alloy exsolution reversibility. **Figure 3d** depicts the HRFSEM micrograph of the Sr₂FeCo_{0.2}Ni_{0.2}Mn_{0.1}Mo_{0.5}O_{6-δ} pellet after the in-situ NAP-XPS, which shows the morphology of the re-oxidized sample, (the 2 h in O₂ re-oxidation treatment was the last step of the in-situ experiment). This figure includes a comparison with the pristine (as prepared) and reduced (after treatment of 4 h at 600 °C in a tubular furnace with 5% H₂/Ar). After the re-oxidation step, the sample lost a significant part of the exsolved NPs, showing the reversible nature of the ternary alloyed FeCoNi exsolved NPs. However, some of the NPs remained on the surface, but with some morphological changes; namely, the remaining NPs appear more polyhedral than the originally spherical-exsolved NPs. This might indicate that, for a complete re-dissolution of all the exsolved NPs back to the



perovskite bulk, longer exposure times or higher temperatures will be required to speed up the process kinetics. The fact that, after re-oxidation, no metallic phases are observed with NAP-XPS indicates that these NPs might be in oxidized form, which might explain the observed morphological alterations.

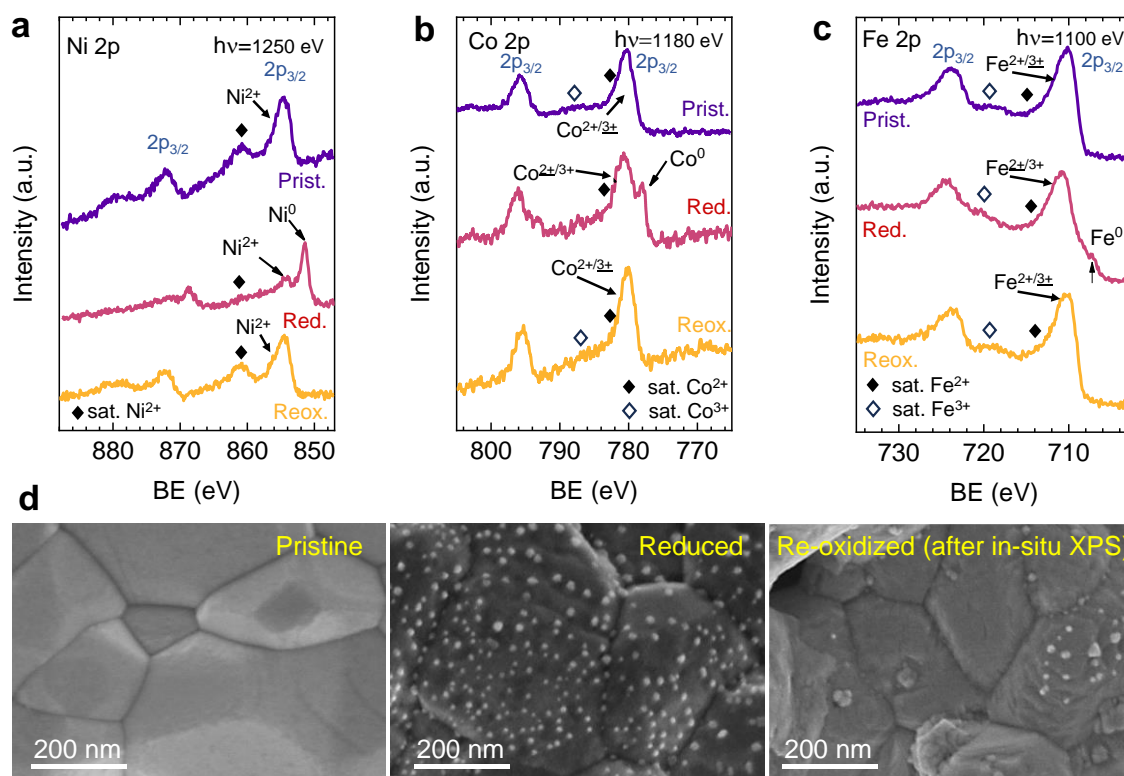


Figure 3: NAP-XPS spectra of (a) Ni 2p, (b) Co 2p, and (c) Fe 2p acquired in-situ at 600 °C in pristine (“Prist.”, 0.2 mbar O₂), reduced (“Red.”, 0.2 mbar H₂) and re-oxidized (“Reox.”, 0.2 mbar O₂) conditions. The used photon energies (to result in a similar electron kinetic energy of ~400 eV) are indicated in the panels. A constant offset for better clarity is added to the spectra. (d) HRFSEM micrographs of Sr₂FeCo_{0.2}Ni_{0.2}Mn_{0.1}Mo_{0.5}O_{6-δ} at pristine, reduced, and re-oxidized stages. The re-oxidized micrograph of the sample was taken after NAP-XPS in-situ experiments.

After observing the exsolution reversibility based on NAP-XPS data of Ni, Co, and Fe, the focus will now be on the analysis of the non-exsolvable lattice elements to understand the overall changes affecting the perovskite surface chemistry under the reducing (exsolution)/oxidizing treatments. **Figure 4** depicts the NAP-XPS spectra of the Mn 2p, O 1s, Mo 3d, and Sr 3d core levels acquired in-situ at 600 °C. Beginning with **Figure 4a**, which shows the Mn 2p photoemission lines: the Mn 2p_{3/2} spectra of the pristine and re-oxidized sample exhibit a major contribution at around 641 eV, ascribed to Mn³⁺. Another minor contribution can be observed at higher BE of around 643 eV, attributed to Mn^{4+58,59}. After reduction, there is a shift to lower BE due to the reduction of Mn^{3/4+} to



Mn²⁺⁴⁶. However, the significant spectral width of Mn 2p_{3/2} and Mn 2p_{1/2} peaks suggests that manganese in the reduced state might in fact be a superposition of spectral features related to 2+ and 3+ oxidation states. Additionally, in **Figure S5a**, the Mn spectra acquired with a lower electron kinetic energy (150 eV) can be seen, revealing a similar structure profile along the host perovskite.

Figure 4b exhibits the Mo 3d core level spectra. In the pristine sample state, the NAP-XPS data reveals that Mo is in the 6+ oxidation state, consistent with the Mo 3d_{5/2} peak at ca. 232 eV⁶⁰. Upon reduction, this peak shifts 1.0 eV to higher BE, ascribed to the change in oxygen partial pressure (this is also clearly observed for O 1s and Sr 3d spectra)³⁰. In addition, in the reduced form, the intensity decreases, and a second peak appears, which is related to Mo⁵⁺⁶⁰, as Mo is partially reduced under exsolution treatment conditions. To quantify the amount of Mo⁶⁺ that gets reduced to Mo⁵⁺, all the Mo 3d spectra were fitted following the work of Spevack and McIntyre⁶⁰. **Figure S6** shows all the fitted spectra for the pristine, reduced and re-oxidized sample states using three photon energies: 380, 630 and 930 eV. These photon energies were applied to result in 150, 400 and 700 eV electron kinetic energies, respectively. Nevertheless, those are approximate values, and the exact electron kinetic energies employed might be shifted in order to avoid Auger signal overlaying. In the pristine and re-oxidized sample state, only Mo⁶⁺ is present at the surface of the double perovskite. In the reduced sample state and for the three photon energies assessed, Mo⁵⁺ 3d_{5/2} and 3d_{3/2} peaks appear at 231.9 and 235.05 eV, respectively. The Mo⁵⁺/Mo_{total} ratio was 0.48, 0.49, and 0.48 when acquired with 380, 630 and 930 eV photon energies, respectively. This indicates that, during the exsolution process that took place under these conditions (600 °C, 0.2 mbar H₂), almost half the Mo⁶⁺ surface cations were reduced to Mo⁵⁺, regardless of the sampling depth applied. In addition, upon re-oxidation, a full return to the 6+ oxidation state is observed. Despite during 600 °C XRD experiments (1 bar 5% H₂/Ar) no RP phase formation was observed, the H₂ pressure used in NAP-XPS can be determinant to ease the partial phase transformation into RP. So then, that remarkable formation of Mo⁵⁺ might be attributed to the crystallographic phase transformation from double perovskite (with a generic formula Sr₂Fe_{1.5}Mo_{0.5}O₆) into a Ruddlesden-Popper phase (Sr₃FeMoO₇), as previously discussed^{20,34,52}. In Sr₃FeMoO₇, Fe is in +3 state and Mo in +5 oxidation states, which matches well with the extracted results from the NAP-XPS data. Therefore, under the



conditions used for these NAP-XPS experiments, it can be assumed that a significant part of the double perovskite is being transformed at the surface into the RP phase.

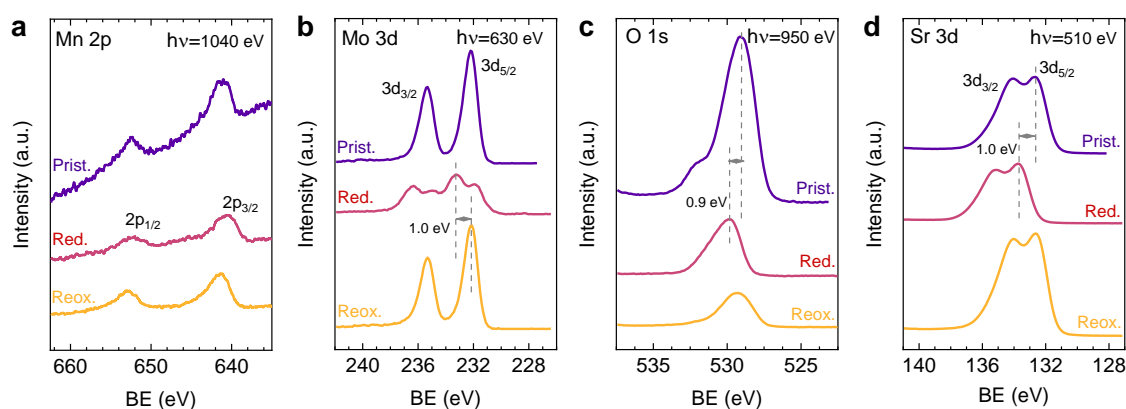


Figure 4. NAP-XPS spectra of (a) Mn 2p, (b) Mo 3d, (c) O 1s, and (d) Sr 3d acquired in-situ at 600 °C in pristine (“Prist.”, 0.2 mbar O₂), reduced (“Red.”, 0.2 mbar H₂) and re-oxidized (“Reox.”, 0.2 mbar O₂) conditions. The used photon energies (to result in a similar electron kinetic energy of ~400 eV) are indicated in the panels. A constant offset for better clarity is added to the spectra.

O 1s and Sr 3d spectra are depicted in **Figures 4c** and **4d**, respectively. Focusing on the O 1s spectra, it shall be noted that the pristine peak intensity is much higher than in the reduced and re-oxidized sample states. In addition, it presents a higher contribution of adsorbed species, as inferred from the signal at 532 eV³⁰. To better understand the changes that O 1s experienced during the redox experiments, a thorough analysis of the NAP-XPS spectra of all the states (pristine, reduced and re-oxidized) acquired with three different photon energies (705, 950 and 1250 eV to result in ca. 150, 400 and 700 eV electron kinetic energies, respectively) is depicted in **Figure 5**. The O 1s XPS spectra were fitted considering three distinct components. The one at 532 eV is attributed to adsorbed oxygen species at the surface or secondary phases⁶¹. The peak at around 530 eV is also considered a surface component, and it is ascribed to oxygen in the surface outer-surface layer of the perovskite structure layer⁶¹. Finally, the low energy component at around 528 eV is attributed to oxygen in the perovskite lattice. As a general trend, the O 1s spectra component deconvolution (**Figure 5**) suggests that increasing the kinetic energy (so then, higher IMFP) shows an increase of the lattice component with respect to the surface species. This is especially evident for the pristine sample state. In the case of the reduced sample state, the spectra were deconvoluted just with the lattice and surface outer-surface layer oxygen since adsorbed species were not inferred. These chemisorbed oxygen species are usually (OH)⁻_{ads}, O⁻_{ads}, and/or O²⁻_{ads}³⁰. Upon re-oxidation under an



oxygen atmosphere, some of these species regenerate (a signal at around 532 eV shows up again). However, in the re-oxidation state, these peaks have less intensity than in the pristine state, suggesting that some of the adsorbed species do not regenerate. This might be the case for $(\text{OH})^-_{\text{ads}}$, which could be present in the pristine sample state but does not regenerate in the dry oxygen conditions employed in the re-oxidation step. Notably, in the pristine sample state, adsorbed carbonaceous species were removed from the surface thanks to the pre-heating stage performed at the beginning of the in-situ experiment (**Figure S3**). This is confirmed in **Figure S7**, which shows the C 1s + Sr 3p core level regions for the pristine sample state. There, only the spin-orbit doublet associated with Sr 3p is observed, whereas no peak at around 284.8 eV that could be associated with carbon-containing species was detected.

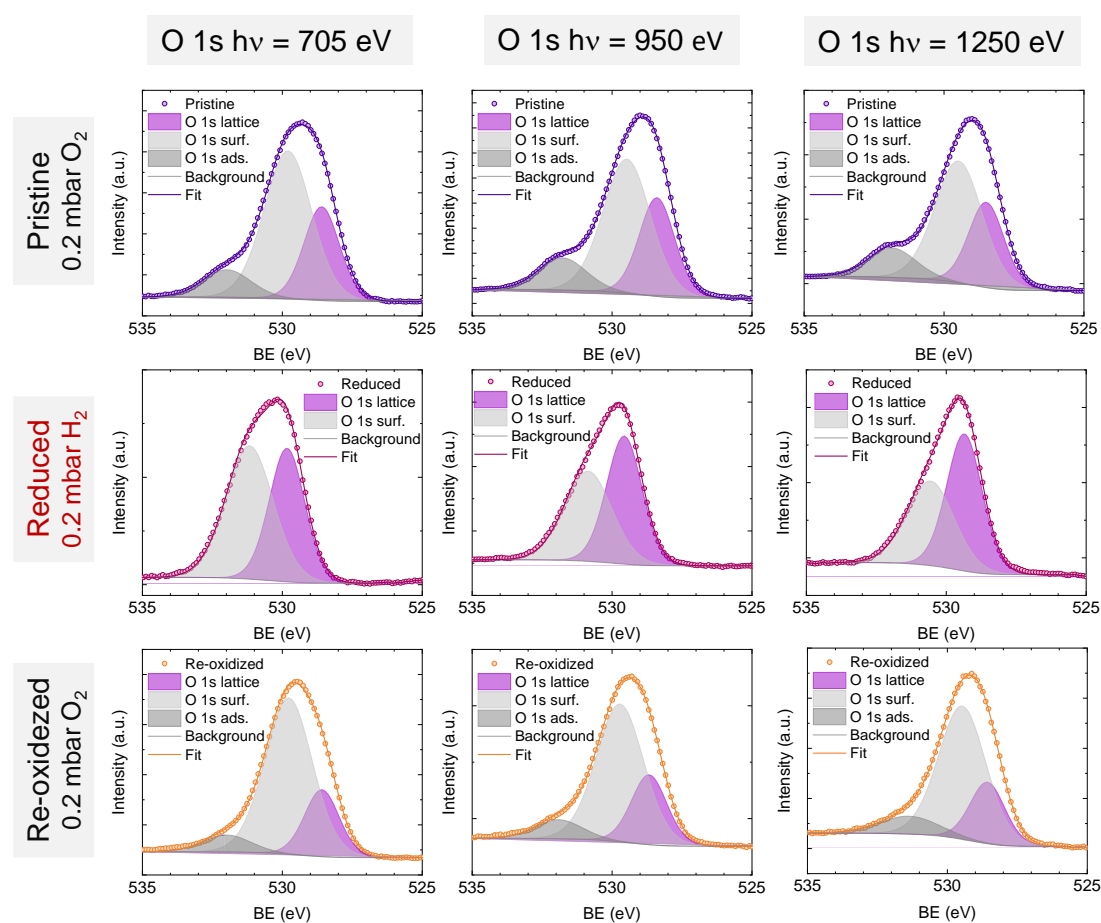


Figure 5. NAP-XPS spectra of O 1s in the pristine (0.2 mbar O_2), reduced (0.2 mbar H_2), and re-oxidized (0.2 mbar O_2) sample states recorded using three photon energies: 705, 950 and 1250 eV.

To understand the variations in the O 1s spectra at each sample state and representing different sampling depths, the surface/bulk ratio was quantified based on the fitted data and plotted against the IMFP in **Figure 7a**. As expected, for the reduced sample state we



find the lowest surface/bulk ratio at every considered IMFP (ca. 0.5, 1.0, and 1.5 nm). This fact is related to the formation of oxygen vacancies ($V_O^{\bullet\bullet}$) during the reducing process. Interestingly, upon re-oxidation, the surface/bulk ratio is increased compared to the pristine sample state, indicating an oxygen enrichment affecting every layer after re-oxidation. The calculated values (ca. 3.0-3.5 nm) are significantly higher than for other studied perovskites, such as $\text{SrTi}_{1-x}\text{Fe}_x\text{O}_3$ ³⁰.

Lastly, **Figure 6** shows the fitted NAP-XPS spectra of the Sr 3d core level for all the studied sample states recorded using 260, 510, and 810 eV photon energies (to result in ca. 150, 400, and 700 eV electron kinetic energies, respectively). The Sr 3d spectra were, in all cases, fitted considering two spin-orbit doublet components: one at lower BE (Sr 3d_{5/2} at ~ 132.2 eV) ascribed to Sr in the perovskite lattice and the high energy doublet (Sr 3d_{5/2} at ~ 133.5 eV) attributed to Sr in the surface⁶¹. In this case, the Sr surface species is most likely SrO or Sr(OH)₂^{30,48} since, as previously mentioned, carbon compounds (such as SrCO₃), were not observed. It is worth mentioning that the width of the surface fit components is broader than the bulk ones (**Figure 6**). This has been previously reported for Sr 3d and it is ascribed to the larger disorder (i.e., different bond lengths and/or angles) affecting the surface components when compared to the bulk³⁰. A similar phenomenon was observed for O 1s (**Figure 5**). The surface/bulk ratio for the Sr species was quantified based on the fitted NAP-XPS spectra and plotted in **Figure 7b**. As a general trend, the surface/bulk ratio decreases with increasing IMFP for every sample state (pristine, reduced, and re-oxidized). For IMFPs of ~0.5 and ~1.0 nm, the surface/bulk ratio is above that in the pristine sample state, suggesting a Sr surface enrichment affecting the outer-surface layer, commonly observed in perovskite oxides^{30,48,61,62}. Increasing the IMFP up to ~1.5 nm decreases the surface/bulk ratio, indicating a less-pronounced Sr enrichment in inner lattice layers. Interestingly, at every considered IMFP, the pristine sample state exhibits the highest surface/bulk ratio, followed by the re-oxidized and, lastly, the reduced sample state. This Sr enrichment for the pristine sample state (for ca. 0.6 and 1.0 nm IMFP) might be due to a presence of segregated SrO³⁰. This phase is most likely amorphous since no evidence of its presence could be detected in the XRD data (see **Figure 1**). These SrO segregations might impact detrimentally the electrocatalytic performance of the electrodes²⁰. Moreover, recently, Riedl et al. highlighted the possible interaction of these Sr segregations with trace amounts of sulfur species, even in high purity gases, which negatively affected to the polarization resistance of the studied cells⁶³.



Upon reduction, this SrO segregation disappears, thus lowering the surface/bulk ratio. After re-oxidation, the Sr surface-to-bulk ratio slightly increases compared to reduced sample state, but never reaches the pristine sample state values. Therefore, the SrO segregated phase presumably does not reform during re-exsolution. It is worth mentioning that both, O 1s and Sr 3d surface/bulk ratios studied suggest a reorganization of the superficial layers of the host double perovskite, which might affect exsolution process during subsequent reductions.

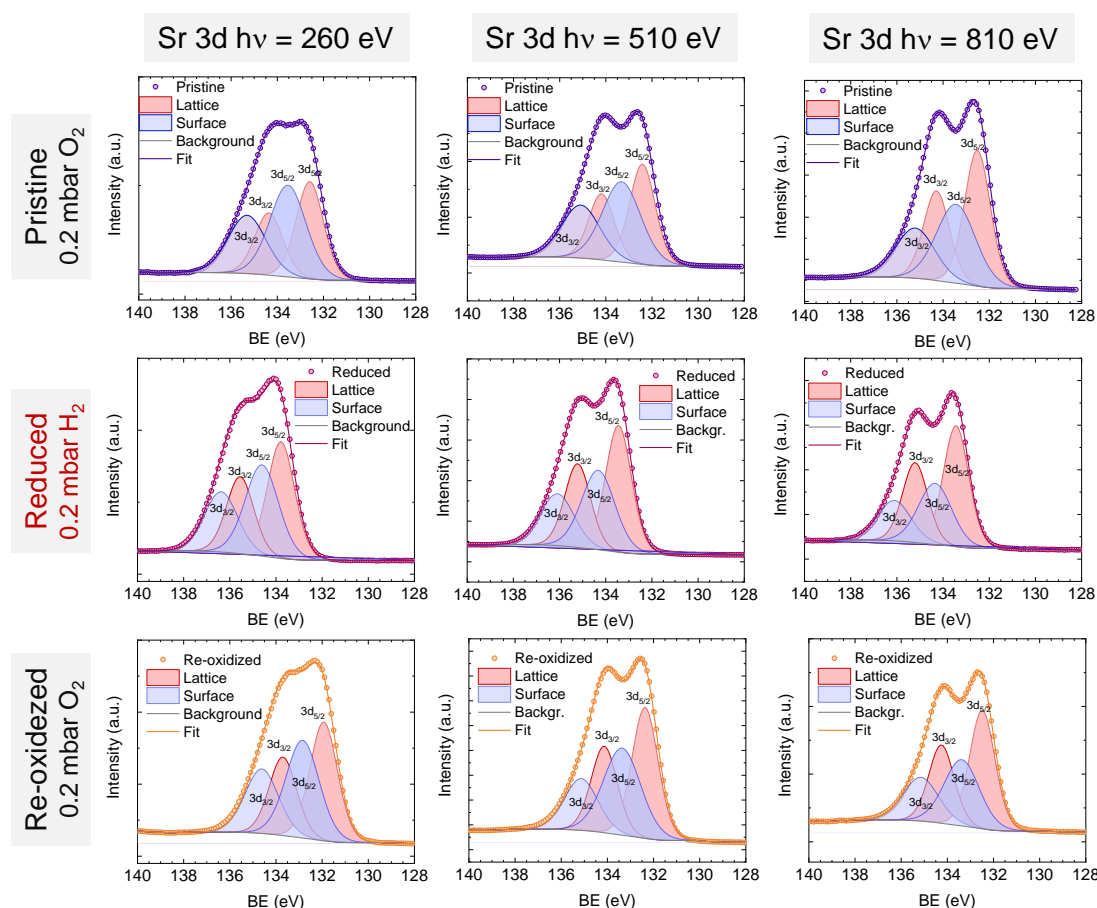


Figure 6. NAP-XPS spectra of Sr 3d at the pristine (0.2 mbar O₂), reduced (0.2 mbar H₂), and re-oxidized (0.2 mbar O₂) sample states recorded using three photon energies: 260, 510, and 810 eV.

Overall, in this section the surface changes associated with the exsolution process have been identified, paying particular attention to the variations suffered by the cations that do not participate in the NP exsolution. This knowledge is paramount since the perovskite surface is key in many relevant electrocatalytic processes.



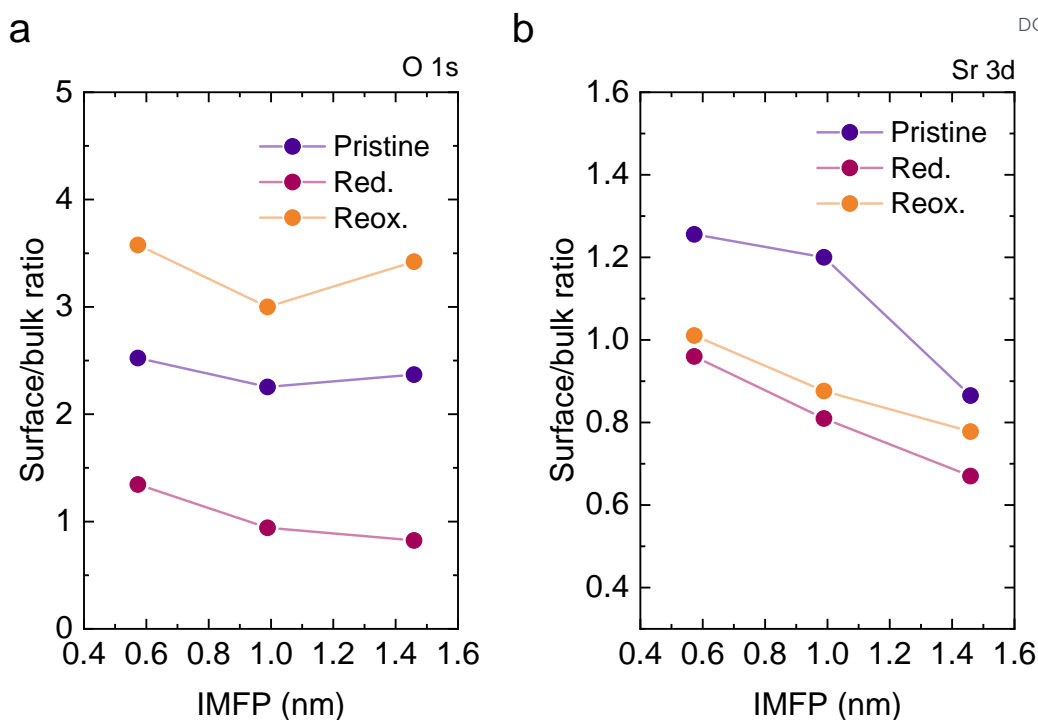


Figure 7. Surface/bulk component ratio of (a) O 1s and (b) Sr 3d, calculated based on NAP-XPS fitted data at each photon energy (705, 950, and 1250 eV for O 1s and 260, 510, and 810 eV for Sr 3d) depicted as a function of the corresponding IMFP.

3.2.2 Monitoring exsolution regeneration with in-situ XRD

Finally, this section evaluates the ability to regenerate the exsolved NPs after reoxidation with in-situ XRD reduction-oxidation cycles. As depicted in **Figure S3**, this set of experiments isothermally studied the formation of exsolved NPs, re-dissolution back to the perovskite bulk under oxidizing conditions, and the regeneration of the exsolved NPs in a second reduction step. These redox experiments were conducted at two different temperatures (600 and 800 °C), atmospheric pressure, and under 5% H₂/Ar (reduction step) or synthetic air (re-oxidation step). **Figure 8** shows the time-resolved variations of the XRD reflections of the Sr₂FeNi_{0.2}Co_{0.2}Mn_{0.1}Mo_{0.5}O_{6-δ} sample at the two aforementioned temperatures. Here, the focus was put on the two most relevant regions, namely: 8.1-8.7 ° region (most intense double perovskite reflection) and 11.1-11.7 ° region (metallic ternary alloyed exsolved NPs reflections). At 600 °C, during the first reduction step of 4 h under 5 % H₂, the oxide exhibits a minor lattice expansion since the main peak shifted to lower 2θ angles (from 8.47 ° to 8.46 °). This might indicate that most of the oxygen vacancies were already formed during the heating up to 600 °C. Next, after the 4-hour reduction treatment, the gas atmosphere was changed to synthetic air. During



the first period in air, the sample did not exhibit any remarkable change until reaching 15 min of exposure to oxygen, when an abrupt shift to higher 2θ values was observed. Namely, the shift occurred from 8.47 to 8.52 °, evidencing a lattice contraction, which is ascribed to the oxygen vacancies replenishment and the oxidation of reduced B-site transition metal cations in the lattice. Finally, the gas was switched back to 5% H₂/Ar for 2 hours. A second remarkable change was observed after 45 minutes of exposure to the reducing atmosphere, corresponding to a shift to lower 2θ angles due to a lattice expansion. Here, the main reflection of the double perovskite shifted back to 8.46 °, being this lattice expansion ascribed to the formation of oxygen vacancies and the reduction of metal transition cations in the lattice. Interestingly, even if both the oxidation and reduction occurred in a very abrupt manner, reduction needed about 45 min to happen, whereas the oxidation took place within 15 minutes of exposure to air atmosphere. Both times are generally longer than what reduction/oxidation reactions of perovskites usually demand. For instance, for chemical looping applications, re-oxidation can take place in less than 5 min at 900 °C⁹. However, we should note here the extremely low gas flow rates of 1 mL/min used in the in-situ XRD setup, which caused a very slow gas exchange in the capillary, increasing the overall time needed to observe the crystallographic changes.

Regarding the 11.1-11.7 ° region, a peak appearing at $2\theta = 11.55$ ° is observed in the first 4-hour reduction step. This peak is ascribed to the formation of metallic Ni from the reduction of NiO impurities (see **Figure 1**). During the 4-hour treatment at 600 °C, this signal did not exhibit any noticeable shift. Upon the change to the oxidizing atmosphere, this metallic Ni phase progressively transitions into NiO (peak at 11.27 °). The onset of this reaction happens also after 15 min exposure to air atmosphere, just like the double perovskite oxidation. Although we have observed ternary alloy exsolution after a 4-hour treatment at 600 °C with HRFSEM and TEM in previous work²⁰, here it was not possible to infer its presence with in-situ XRD, probably hampered by the NiO/Ni impurities redox process. When switching again to the reductive atmosphere in the second treatment under H₂, the NiO phase was reduced to Ni again after 45 min of exposure, coinciding with the double perovskite reduction.



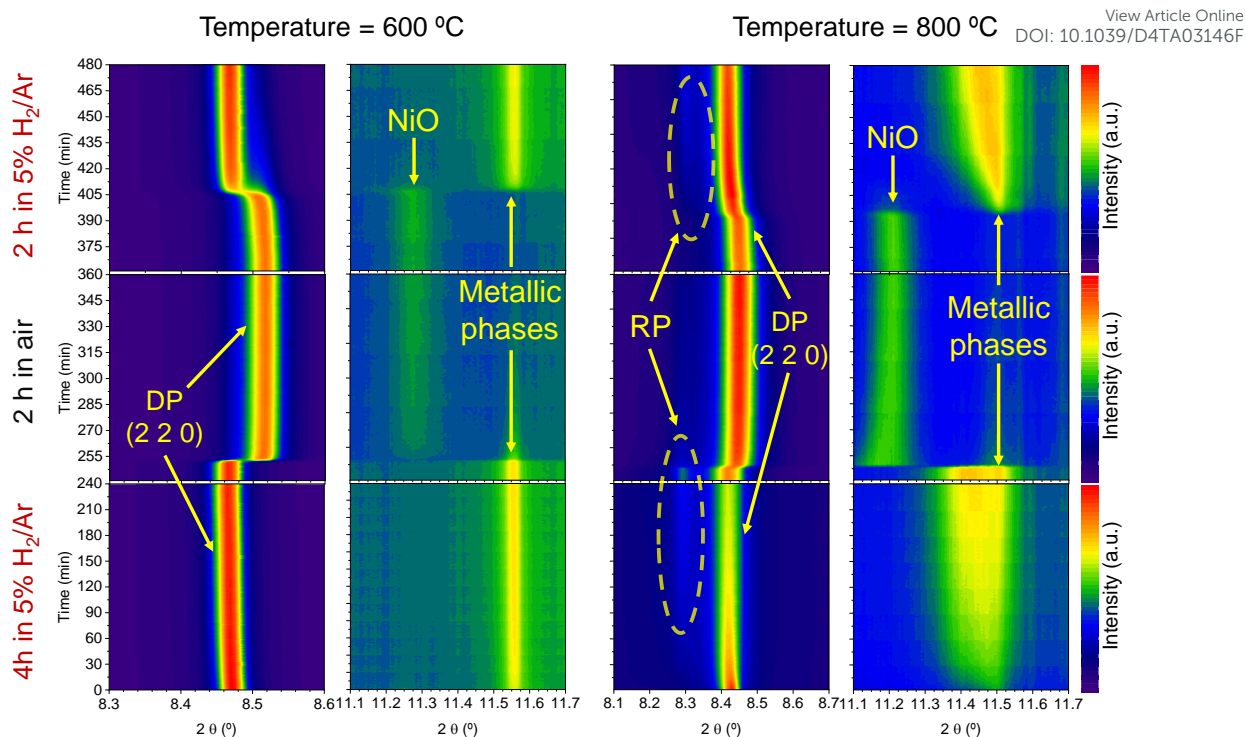


Figure 8. Time-resolved in-situ XRD contour maps for the evaluation of exsolution regeneration. Temperature was raised to either 600 (left panels) or 800 °C (right panels) in 5% H₂/Ar atmosphere. After reaching the target temperature, reduction was carried out for 4 h, followed by an oxidation step of 2 h in synthetic air. Finally, a last reduction step of 2 h was performed by changing the atmosphere back to 5% H₂/Ar. Note that the x-axis scales from the 600 °C and the 800 °C differ for the panels showing low 2θ diffraction patterns. Double perovskite phase and Ruddlesden-Popper phase are labeled as DP and RP, respectively.

The same redox cyclic process was evaluated at 800 °C, finding remarkable differences. First, it was observed that the main reflection of the cubic double perovskite decreased in intensity during the 4-hour reductive treatment, with a concomitant phase transition from double perovskite to an RP phase. This is better observed in **Figure 9a**, where selected diffractograms taken with 30 min intervals are plotted. It can be observed that the RP phase appears after 30 min exposure with a main peak located at 8.3 °. In this 4-hour treatment, the transition to the RP phase is partial, reaching a lower conversion extent if compared with ex-situ analyses after reduction in a tubular furnace²⁰. After changing to the oxidation step, firstly, the RP phase disappears, and secondly, the double perovskite main peak shifts to higher angles. Thus, the transformation between double perovskite and RP phases is reversible, which is consistent with previous reports³⁴. In this case, the transformation occurred during 7.5 min of exposure to air, while at 600 °C it took 15 min, indicating that the increase in temperature helped also in speeding up the redox transitions. This event was also observed in the second reduction step. Here, the abrupt



shift to lower 2θ values happened after ~ 30 min under reducing conditions, together with the RP formation onset. **Figure S8** compares the main reflections after the last 2-hour reduction step for both 600 and 800 °C. It can be observed that at 800 °C, the peak intensity is lower than at 600 °C, it appears at lower 2θ values (higher reduction extent at higher temperatures), and the presence of the RP phase, reflecting the remarkable impact of the temperature increase on the exsolution process, which ultimately affect the electrochemical properties and durability of the electrode²⁰. It is worth noting that, in the same figure, some slight signal can be seen at around $2\theta = 8.35^\circ$, which might indicate the slight formation of RP phase at 600 °C after the second reduction step, not observed during the 4-hour reduction period. Nevertheless, this peak appears in almost negligible amounts.

Figure 9b depicts the 11.1 - 11.7° region, where metallic phases associated with the ternary alloy exsolution are expected to appear. At the beginning of the isothermal 4-hour treatment, an asymmetric reflection is already observed between 11.35 and 11.55° . By increasing the exposure time, the reflection exhibits changes affecting the region around 11.47° and later affecting the region around 11.40° . The former is ascribed to the growth of the exsolved ternary alloyed NPs, whereas the latter corresponds to the $(0\ 0\ 10)$ reflection of the RP phase (the growth of this minor RP reflection is simultaneous to the one observed in **Figure 9a**). The minor initial peak observed at 11.55° is ascribed to metallic Ni originating from the reduction of NiO impurities, whereas, at 11.50° , the exsolved metallic phase can already be observed. **Figure 9b** indicates that the major exsolved NP growth occurs at the early stages of the isothermal reduction process, namely in the first 30 minutes. As commented in section 3.1.1, the nucleation of the exsolved NPs already occurred during the heating stage under reducing conditions (**Figure 1**). Thus, it is expected that time will mainly play a key role in the growth and/or consolidation of the already existing exsolved NPs rather than in forming new ones.



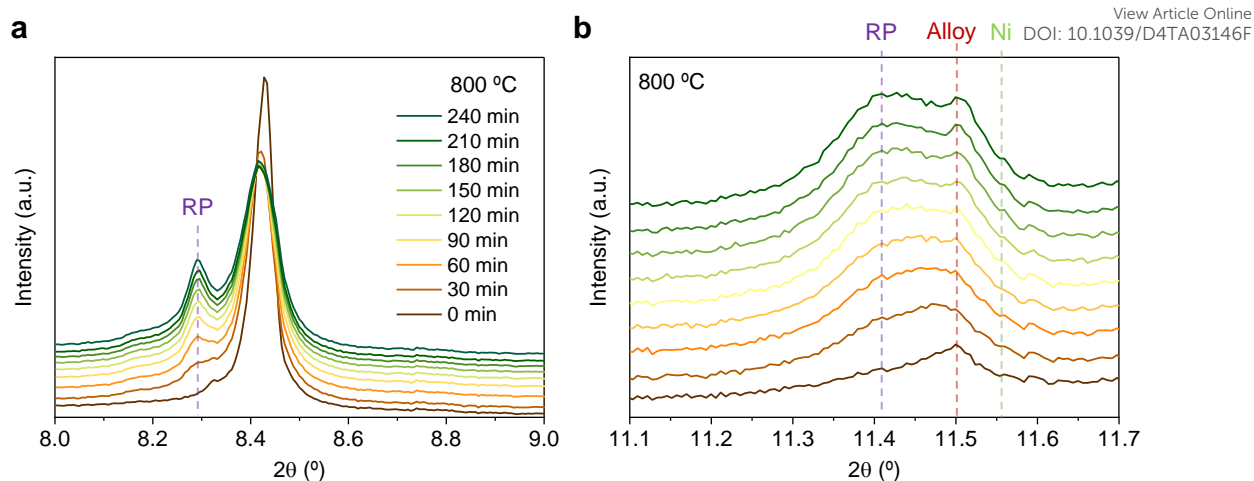


Figure 9. Time-resolved in-situ XRD at 800 °C, during the first reduction step in 5% H₂/Ar for (a) the 8-9 ° region and (b) the 11.1-11.7 ° region, exhibiting the formation of the Ruddlesden-Popper phase (RP), the exsolution of ternary alloyed NPs and the emergence of Ni caused by the reduction of minor NiO impurities.

After the initial 4-hour reduction step, changes affecting the metallic phases were studied in the subsequent re-oxidation and second reduction treatments. **Figure 10a** depicts this 2-hour re-oxidation step. Overall, it is a very fast process. Just after 5 min, the region associated (~11.4 °) with the (0 0 10) RP reflection illustrates that this phase remarkably decreases its presence and totally vanishes after 10 minutes, confirming that the oxidation of RP to double perovskite is much faster than the reverse path. Additionally, after 5 re-oxidation minutes, a broad peak appears between 11.1 and 11.3 °, which centers around 11.2 °. The fact that this peak is rather broad might indicate the presence of two different oxidized species emerging simultaneously. One would be NiO from the oxidation of Ni-segregated impurities, as already observed in the experiments at 600 °C (**Figure 8**). The second one could be ascribed to oxidation of the exsolved NPs, so the exsolved ternary alloys are partly re-oxidized during the initial stages of the re-oxidation. Only slight differences were observed between 10- and 120-min exposure in the diffraction patterns (**Figure 10a**). First, the peak at around 11.2 ° progressively increases, indicating NiO formation due to re-oxidation, suggesting a non-complete re-dissolution of Ni metallic species. Secondly, in the 2θ region between 11.5-11.6 °, it is observed that the signals associated with the FeCoNi exsolved NPs and Ni⁰ narrow but are not completely gone. This indicates that the 2-hour re-oxidation was insufficient for a complete re-dissolution of the metallic exsolved NPs back to the perovskite lattice, especially for Ni. It is worth mentioning that the in-situ XRD setup might be conditioning these results. Low gas flows (1 mL/min) were introduced through the packed oxide powder in the capillary. This fact



might cause preferential paths, hence hampering total re-oxidation of the exsolved NPs, explaining the minor metallic signals remaining. This adequately correlates with the HRFSEM micrographs taken after the in-situ NAP-XPS re-oxidation, where, in some areas, exsolved NPs were still present (**Figure 3d**). The precise composition of these remaining NPs and further morphological changes under reduction/oxidation cycles will be explored in section 3.2.3. Using similar compositions, using in-situ HRFSEM, Lv et al. found that, before total re-dissolution, CoFe alloys formed CoFeO_x nanosheets as an intermediate step³⁴. In this line, Santaya et al. observed that, after 1 h oxidation, FeNi_3 exsolved NPs transform in Ni-rich ($\text{Ni}_{0.9}\text{Fe}_{0.1}$)O oxide NPs over the surface. The authors also explained that after 24-hour oxidation, the surface was free of NPs³⁰. Therefore, it seems that exsolved NP oxidation is an intermediate step before total re-dissolution to the host oxide, which is time (and temperature) dependent and might also be conditioned by the material.

Finally, **Figure 10b** shows the changes occurring during the second reduction step, that is, the re-exsolution experiment. It should be noted here that this exsolution treatment is performed purely isothermally, while in section 3.1.1, the formation of ternary alloyed exsolved NPs began while applying a heating ramp. This might have some relevant implications for the NP's growth, as recently reported by Santaya et al.³⁶, who analyzed isothermal vs stepwise reduction paths, finding remarkable differences in the amount of metallic Fe exsolved, NP size, population, and even in Sr segregations. This might, in turn, explain the slight differences in the peak shapes when comparing the diffractograms after the first and second reduction treatments. Namely, during the first treatment there was always a sharp peak termination at 11.50° (**Figure 9b**). However, during the second treatment, the signal, starting at 11.50° in the initial exsolution stages, shifts to 11.45° at the end of the 2-hour reduction (**Figure 10b**). This shift might be related to alterations in the NP composition that occur during the exsolution process. This aspect will be explored in more detail in the following section.



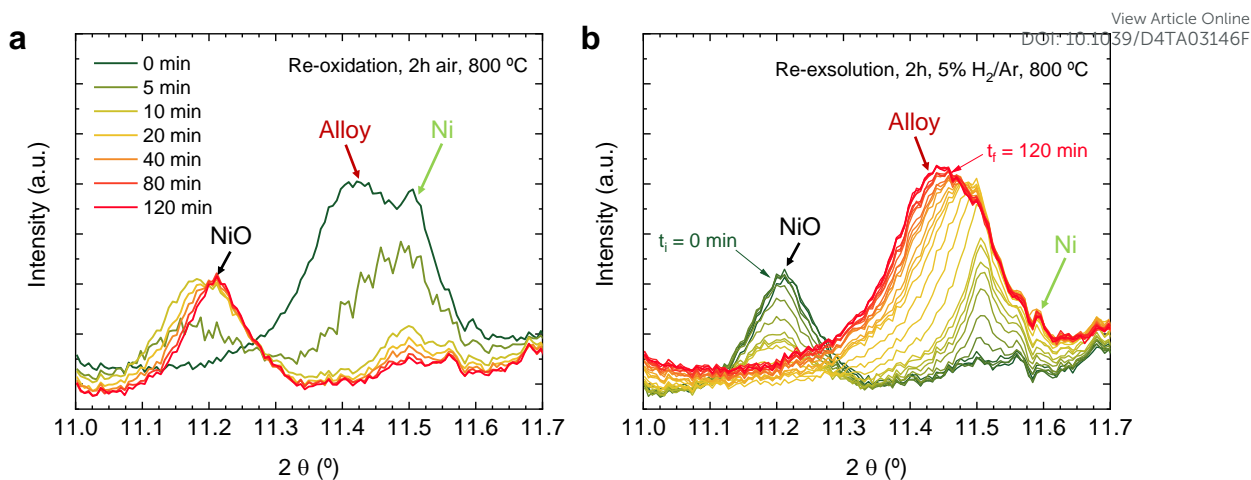


Figure 10. Time-resolved in-situ XRD at 800 °C, during (a) the re-oxidation step of 2 h under air atmosphere followed by (b) the second reduction step in 5% H₂/Ar for the region between 11.1–11.7 °.

3.2.3 Compositional and morphological changes upon reversible exsolution

Ex-situ redox treatments were carried out to explore morphological and/or compositional changes affecting the exsolved NPs. After the first exsolution, characterizations of the material were performed after 2 and 10 h re-oxidation. It is worth mentioning, after 2 hours of re-oxidation, part of the material was taken out for characterization purposes and the rest was re-introduced in the furnace for ongoing oxidation, until reaching the 10 hours. The same procedure was done between 10 and 24-hour re-oxidations. Finally, the 24 h re-oxidized material was subjected to re-exsolution. HRFSEM micrographs of the material after each redox step can be seen in **Figures 11a-e**. As expected, after the first exsolution (**Figure 11a**), spherical well-dispersed NPs are observed over the surface of the material (having a mean size of 22.5 nm). During re-oxidation, exsolved NPs gradually re-dissolve back into the parental oxide (**Figures 11b-d**). After 2 h re-oxidation, **Figure 11b**, despite most of the NPs were re-dissolved, some can still be observed at the surface, but with notable morphological changes. The remaining ones exhibit a polyhedral shape instead of spherical, which may suggest specific compositional changes. This fact is corroborated via XEDS map scans (**Figure 11f**) and line scans (**Figure 11g**), which confirmed that the observed NPs are no longer metallic but mainly composed of Ni oxides. Despite the original exsolved NPs being composed of a ternary FeCoNi alloy, no significant amount of Fe or Co can be seen after 2 h oxidation, suggesting a slower re-dissolution of Ni. These results are consistent with the time-resolved in-situ XRD analyses (**Figures 8 and 10a**) performed at 800 °C, where NiO signal emerges during 2 h re-oxidation treatment. The population of these Ni oxide NPs narrows progressively over



time until almost no NP can be seen after 24 h of treatment (**Figure 11d**). Interestingly, during the re-dissolution process, some remarkable surface morphological phenomena are taking place, affecting the surroundings of the NPs. More specifically, some of the NPs appear to be sunk in superficial holes, gradually disappearing with oxidation time increase, leaving these holes empty (especially visible after 10 h re-oxidation, **Figure 11c**). Finally, once metals are fully re-dissolved, the superficial appearance of the parental metal oxide is recomposed, and no holes can be appreciated (**Figure 11d**). This fact suggests a reorganization of the surface of the host metal oxide around the NPs during re-oxidation and the consequent re-dissolution of metallic cations.

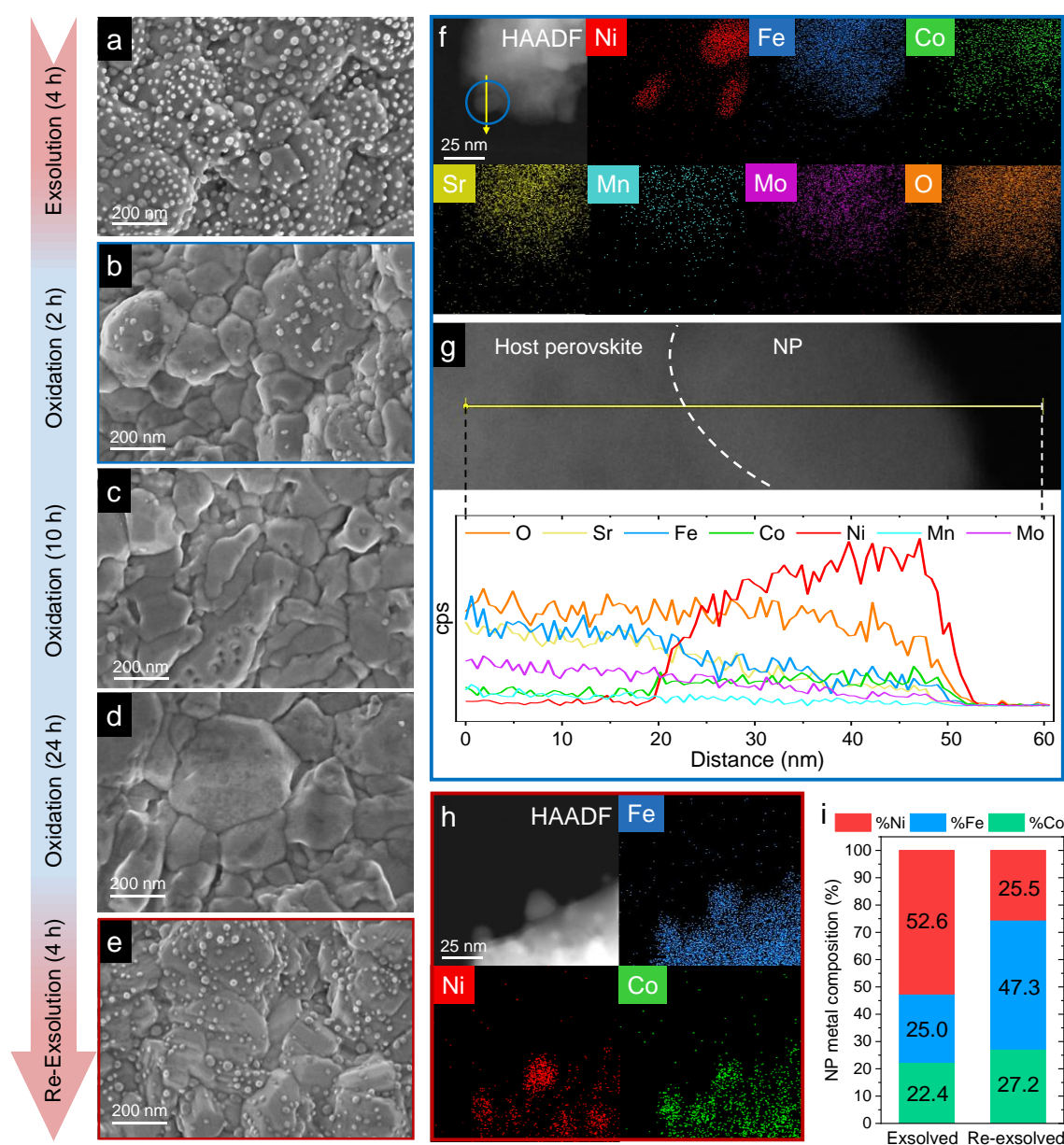
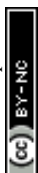


Figure 11. HRFESM micrographs of Sr₂FeCo_{0.2}Ni_{0.2}Mn_{0.1}Mo_{0.5}O_{6-δ} after ex-situ 800 °C, 4 h exsolution in 5% H₂/Ar flow (a). The same sample after re-oxidation at 800 °C in air for 2 (b), 10 (c), and 24 h (d).



Following the 24 h re-oxidation, another reduction treatment (800 °C, 4 h, 5% H₂/Ar) was performed for re-exsolution (e). HAADF and XEDS map images of the material after 2 h re-oxidation treatment (f) and line-scan analysis (yellow arrow) for one of the NPs, highlighted in blue (g). These compositional analyses reveal that, after re-oxidation, the remaining NPs are mainly composed of NiO. HAADF and map images of re-exsolved NPs, revealing that after re-exsolution ternary FeCoNi ternary alloys are also obtained (h). Compositional comparison of the exsolved NPs after first exsolution and re-exsolution (i). Compositional information of the first exsolution NPs were taken with permission from Ref.²⁰

After re-oxidation, re-exsolution was performed for 4 h at 800 °C, resulting in the emergence of new spherical NPs spread along the surface of the material (Figure 11e). However, these NPs are morphologically and compositionally different from the original exsolved ones. Firstly, the exsolution extent narrows after re-exsolution since the mean size of the NPs is lower (22.5 versus 14.7 nm), and so does the population (612 against 471 μm^{-2} after the first exsolution and re-exsolution, respectively). NP mean size distribution histograms for both treatments are depicted in Figure S9. Regarding their composition, ternary FeCoNi alloyed NPs are, again, obtained according to XEDS analyses (Figure 11h) but with remarkably different composition ratios (Figure 11i, Figure S10). Namely, the re-exsolved NPs main component is Fe (47.3%) instead of Ni (25.5%), making a notable difference with the original exsolved NPs (25.0 and 52.6% of Fe and Ni, respectively). At the same time, the Co content exhibits no significant alterations (27.2 and 22.4% for re-exsolved and exsolved NPs, respectively). So then, despite the NAP-XPS in-situ data that suggested faster migration kinetics during the exsolution process for Ni (Figure 2d), Fe exhibited higher exsolution rates after re-oxidation and subsequent re-exsolution. This Fe-enrichment found by XEDS-TEM might be related to the observed shift to lower 2θ values affecting the metallic peak when compared to the first exsolution in the time-resolved in-situ XRD analyses (Figure 10b). Indeed, this shift indicates that the compositional change is accompanied by a lattice expansion, which, based on the work of Santaya et al.³⁶, might be explained by a gradual increase in Fe concentration in the metallic NP. This makes sense if considering, for instance, the different lattice volumes for the cubic structures of Ni (41.97 Å³) and FeNi₃ (43.26 Å³). In this case, Fe incorporation in the metallic phase causes a lattice expansion concerning a Ni-rich composition. Thus, the obtained results in this isothermal exsolution at 800 °C suggest that ternary alloy exsolution is followed by a Fe enrichment during the 2-hour treatment, leading to a different final ternary alloy composition, confirming the XEDS observations. The surface re-arrangement occurring during exsolution and later re-



oxidation might trigger the morphological and compositional changes in the re-exsolved NPs (**Figure 12**). In Santaya et al. previous work, a re-arrangement based in a Sr and O enrichment of the outer-surface layer during re-oxidation (after FeNi alloyed NPs exsolution) is suggested³⁰. In this work, an O-enrichment has been also reported after re-oxidation compared to pristine state (**Figure 7a**), which does not apply for Sr (**Figure 7b**). Upon re-oxidation, however, Fe is fully reincorporated into the host perovskite, whereas part of the Ni remains on the surface as Ni-rich oxidized NPs (almost fully reincorporated after long oxidation times). This fact might have an impact in terms of a Fe-enrichment of the outer-surface layer of the host perovskite (**Figure 11g**). So then, the described re-arrangement definitely affects the outmost atomic layers (the ones involved with the exsolution process) of the host perovskite, thus conditioning the latter re-exsolution.

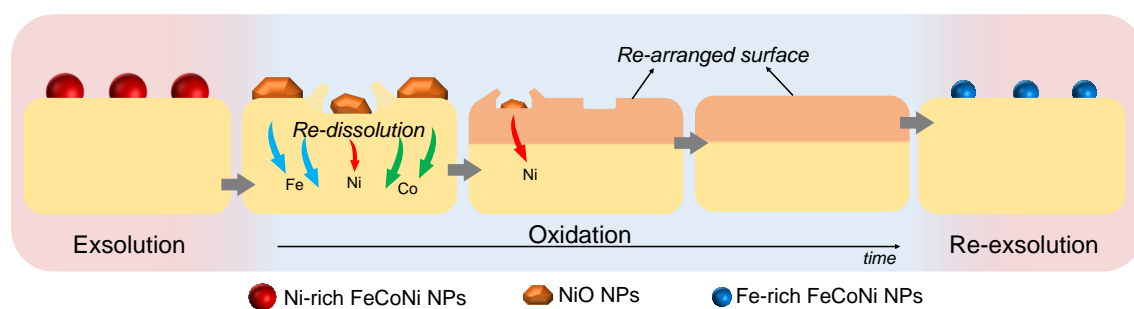
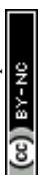


Figure 12. Schematic representation of the ex-situ redox processes affecting the exsolved NPs in $\text{Sr}_2\text{FeCo}_{0.2}\text{Ni}_{0.2}\text{Mn}_{0.1}\text{Mo}_{0.5}\text{O}_{6-\delta}$, and their latter re-dissolution and re-exsolution.

In summary, the mechanistic insights obtained in the present work expand the design space of multielemental nanoparticle exsolution, which could have profound implications in several applications for renewable energy storage and conversion. Here, we have demonstrated that exsolution reversibility comes at the cost of a compositional re-arrangement. This property could be wisely engineered to circumvent the initial observations in which cations with more favorable migration properties (e.g. Ni) were in higher concentration, whereas after redox cycling, one could tune the composition to have a higher content of Fe. This will be especially useful for processes in which metallic Fe is the active species, such as ammonia synthesis or cracking. This is highly relevant since, currently, many works delve into the use of ammonia as a hydrogen carrier to be used as fuel in fuel cells⁶⁴. Hence, the composition of the multicomponent exsolved nanoparticles could be designed *à la carte* by applying a series of redox treatments or by adjusting the process conditions (time, temperature, pressure) to obtain a targeted compound.



Conclusions

View Article Online
DOI: 10.1039/D4TA03146F

In this work, the exsolution, re-dissolution, and regeneration of ternary alloyed nanoparticles were monitored using synchrotron-based in-situ NAP-XPS and XRD measurements. In addition, special attention was paid to crystallographic and surface transformations occurring during the exsolution/re-dissolution process. Both NAP-XPS and XRD revealed the formation of the ternary alloy nanoparticles during a temperature-programmed heating step under reducing conditions. Contrary to some mechanistic literature reports, the exsolution studied here apparently was not driven by the isolated migration of each cation followed by alloying in the surface. However, nucleation sites, which might be induced by the more reducible Ni cations, tended to form along the heating step, leading to nanoparticle growth during the following temperature-dwelling step. Consistent with STEM-XEDS results, the NAP-XPS data showed a higher concentration of metallic Ni species, followed by Co and Fe. Additionally, the presence of Mo^{5+} suggested by NAP-XPS also confirmed the partial crystallographic transformation of the double perovskite phase into a Ruddlesden-Popper structure, which was also inferred by in-situ XRD. This transformation is fully reversible upon re-oxidation re-reduction cycles, being the oxidation from the Ruddlesden-Popper phase to the double perovskite a much faster process than the reduction. Ternary alloyed nanoparticle re-dissolution was confirmed by NAP-XPS, XRD, and HRFESEM, although under the employed conditions in this work, full nanoparticle re-dissolution back to the perovskite was not achieved. In this process, oxidized intermediate phases were detected, acting as a previous step in the exsolved nanoparticle re-dissolution. Nanoparticle re-exsolution was also observed by in-situ XRD. Interestingly, performing the exsolution process isothermally induced changes in the metallic peak positions assigned to the exsolved nanoparticles, suggesting compositional variations throughout the re-exsolution process. This was corroborated by ex-situ redox experiments via XEDS analyses, pointing to an NP Fe-enrichment after re-exsolution. Overall, the results presented here shed light on the detailed crystallographic and surface chemistry changes occurring in the exsolution of ternary alloyed nanoparticles. This knowledge can be used to optimize alloy exsolution in double perovskite electrodes and, in turn, improve their electrocatalytic properties.



Acknowledgements

View Article Online
DOI: 10.1039/D4TA03146F

The project that gave rise to these results received the support of a fellowship from “la Caixa” Foundation (ID 100010434). The fellowship code is LCF/BQ/PI20/11760015. Financial support by Generalitat Valenciana (CIPROM/2022/10) and by the Spanish Ministry of Science and Innovation (PID2022-139663OB-100 and CEX2021-001230-S grants funded by MCIN/AEI/10.13039/501100011033). We thank the financial support of the Helmholtz Initiative and Networking Fund through the HZB-BASF project ENERCHEM: Energiespeicherung durch Chemie. These experiments were performed at BL24-CIRCE (proposal number 2022035801) and BL04-MSPD (2022025687) beamlines at ALBA Synchrotron with the collaboration of ALBA staff. The authors thank Alexander Missyul for the help with setting up the in-situ XRD experiments and Elena Vicente for the support on the NAP-XPS experimental campaign. Authors acknowledge the use of instrumentation as well as the technical advice provided by the National Facility ELECMI ICTS, node "División de Microscopía Electrónica" at Universidad de Cádiz and project PID2022-142312NB-I00. We thank the support of the Electronic Microscopy Service of the Universitat Politècnica de València.



References

View Article Online
DOI: 10.1039/D4TA03146F

- 1 K. Kousi, C. Tang, I. S. Metcalfe and D. Neagu, *Small*, 2021, **17**, 2006479.
- 2 J. H. Kim, J. K. Kim, J. Liu, A. Curcio, J.-S. Jang, I.-D. Kim, F. Ciucci and W. Jung, *ACS Nano*, 2021, **15**, 81–110.
- 3 J. Zhang, M. M.-R. Gao and J.-L. Luo, *Chem. Mater.*, 2020, **32**, 5424–5441.
- 4 D. Neagu, J. T. S. Irvine, J. Wang, B. Yildiz, A. K. Opitz, J. Fleig, Y. Wang, J. Liu, L. Shen, F. Ciucci, B. A. Rosen, Y. Xiao, K. Xie, G. Yang, Z. Shao, Y. Zhang, J. Reinke, T. A. Schmauss, S. A. Barnett, R. Maring, V. Kyriakou, U. Mushtaq, M. N. Tsampas, Y. Kim, R. O’Hayre, A. J. Carrillo, T. Ruh, L. Lindenthal, F. Schrenk, C. Rameshan, E. I. Papaioannou, K. Kousi, I. S. Metcalfe, X. Xu and G. Liu, *J. Phys. Energy*, 2023, **5**, 031501.
- 5 A. J. Carrillo and J. M. Serra, *Catalysts*, 2021, **11**, 741.
- 6 S. Joo, K. Kim, O. Kwon, J. Oh, H. J. Kim, L. Zhang, J. Zhou, J. Wang, H. Y. Jeong, J. W. Han and G. Kim, *Angew. Chemie Int. Ed.*, 2021, **60**, 15912–15919.
- 7 M. A. Naem, P. M. Abdala, A. Armutlulu, S. M. Kim, A. Fedorov and C. R. Müller, *ACS Catal.*, 2020, **10**, 1923–1937.
- 8 Y. H. Kim, Y. Kang, S. Jo, H. Jeong, D. Neagu and J. Myung, *Chem. Eng. J.*, 2022, **441**, 136025.
- 9 A. J. Carrillo, K. J. Kim, Z. D. Hood, A. H. Bork and J. L. M. Rupp, *ACS Appl. Energy Mater.*, 2020, **3**, 4569–4579.
- 10 S.-K. Otto, K. Kousi, D. Neagu, L. Bekris, J. Janek and I. S. Metcalfe, *ACS Appl. Energy Mater.*, 2019, **2**, 7288–7298.
- 11 K. Kousi, D. Neagu, L. Bekris, E. I. Papaioannou and I. S. Metcalfe, *Angew. Chemie Int. Ed.*, 2020, **59**, 2510–2519.
- 12 K. Kousi, D. Neagu, L. Bekris, E. Cali, G. Kerherve, E. I. Papaioannou, D. J. Payne and I. S. Metcalfe, *J. Mater. Chem. A*, 2020, **8**, 12406–12417.
- 13 A. J. Carrillo, L. Navarrete, M. Laqdiem, M. Balaguer and J. M. Serra, *Mater. Adv.*, 2021, **2**, 2924–2934.



- 14 V. Kyriakou, R. K. Sharma, D. Neagu, F. Peeters, O. De Luca, P. Rudolf, A. Pandiyan, W. Yu, S. W. Cha, S. Welzel, M. C. M. Sanden and M. N. Tsampas, *Small Methods*, 2021, **2100868**, 2100868. View Article Online
DOI: 10.1039/D4TA03146F
- 15 X. Li, L. Dai, Z. He, W. Meng, Y. Li and L. Wang, *Sensors Actuators B Chem.*, 2019, **298**, 126827.
- 16 X. Li, L. Dai, Z. He, W. Meng, Y. Li and L. Wang, *Sensors Actuators B Chem.*, 2019, **298**, 126854.
- 17 J. Spring, E. Sediva, Z. D. Hood, J. C. Gonzalez-Rosillo, W. O’Leary, K. J. Kim, A. J. Carrillo and J. L. M. Rupp, *Small*, 2020, **16**, 2003224.
- 18 D. Neagu, T.-S. Oh, D. N. Miller, H. Ménard, S. M. Bukhari, S. R. Gamble, R. J. Gorte, J. M. Vohs and J. T. S. Irvine, *Nat. Commun.*, 2015, **6**, 8120.
- 19 A. J. Carrillo, A. López-García, B. Delgado-Galicia and J. M. Serra, *Chem. Commun.*, , DOI:10.1039/D4CC01983K.
- 20 A. López-García, L. Almar, S. Escolástico, A. B. Hungría, A. J. Carrillo and J. M. Serra, *ACS Appl. Energy Mater.*, 2022, **5**, 13269–13283.
- 21 D. Neagu, V. Kyriakou, I. L. Roiban, M. Aouine, C. Tang, A. Caravaca, K. Kousi, I. Schreur-Piet, I. S. Metcalfe, P. Vernoux, M. C. M. Van De Sanden and M. N. Tsampas, *ACS Nano*, 2019, **13**, 12996–13005.
- 22 C. Tang, K. Kousi, D. Neagu and I. S. Metcalfe, *Chem. – A Eur. J.*, 2021, **27**, 6666–6675.
- 23 K. Zhu, T. Wu, M. Li, R. Lu, X. Zhu and W. Yang, *J. Mater. Chem. A*, 2017, **5**, 19836–19845.
- 24 A. I. Tsotsias, B. Ehrhardt, B. Rudolph, L. Nodari, S. Kim, W. Jung, N. D. Charisiou, M. A. Goula and S. Mascotto, *ACS Nano*, 2022, **16**, 8904–8916.
- 25 E. I. Papaioannou, D. Neagu, W. K. W. Ramli, J. T. S. Irvine and I. S. Metcalfe, *Top. Catal.*, 2019, **62**, 1149–1156.
- 26 Y. F. Sun, J. H. Li, L. Cui, B. Hua, S. H. Cui, J. H. Li and J. L. Luo, *Nanoscale*, 2015, **7**, 11173–11181.
- 27 D. Papargyriou, D. N. Miller and J. T. S. Irvine, *J. Mater. Chem. A*, 2019, **7**,



- 15812–15822.
- 28 T. Zhu, H. E. Troiani, L. V. Mogni, M. Han and S. A. Barnett, *Joule*, 2018, **2**, 478–496.
- 29 H. Lv, L. Lin, X. Zhang, D. Gao, Y. Song, Y. Zhou, Q. Liu, G. Wang and X. Bao, *J. Mater. Chem. A*, 2019, **7**, 11967–11975.
- 30 M. Santaya, C. E. Jiménez, H. E. Troiani, E. A. Carbonio, M. D. Arce, L. M. Toscani, R. Garcia-Diez, R. G. Wilks, A. Knop-Gericke, M. Bär and L. V. Mogni, *J. Mater. Chem. A*, 2022, **10**, 15554–15568.
- 31 B. Delgado-Galicia, A. López-García, A. J. Carrillo and J. M. Serra, *Solid State Ionics*, 2024, **410**, 116532.
- 32 W. Zhang, H. Wang, K. Guan, J. Meng, Z. Wei, X. Liu and J. Meng, *ACS Appl. Mater. Interfaces*, 2020, **12**, 461–473.
- 33 S. Liu, K. T. Chuang and J. L. Luo, *ACS Catal.*, 2016, **6**, 760–768.
- 34 H. Lv, L. Lin, X. Zhang, Y. Song, H. Matsumoto, C. Zeng, N. Ta, W. Liu, D. Gao, G. Wang and X. Bao, *Adv. Mater.*, 2020, **32**, 1906193.
- 35 M. Santaya, H. E. Troiani, A. Caneiro and L. V. Mogni, *ACS Appl. Energy Mater.*, 2020, **3**, 9528–9533.
- 36 M. Santaya, C. E. Jiménez, M. D. Arce, E. A. Carbonio, L. M. Toscani, R. Garcia-Diez, A. Knop-Gericke, L. V. Mogni, M. Bär and H. E. Troiani, *Int. J. Hydrogen Energy*, 2023, **48**, 38842–38853.
- 37 Y. Jiang, Y. Yang, C. Xia and H. J. M. Bouwmeester, *J. Mater. Chem. A*, 2019, **7**, 22939–22949.
- 38 B.-W. Zhang, M.-N. Zhu, M.-R. Gao, X. Xi, N. Duan, Z. Chen, R.-F. Feng, H. Zeng and J.-L. Luo, *Nat. Commun.*, 2022, **13**, 4618.
- 39 H. Tanaka, M. Taniguchi, M. Uenishi, N. Kajita, I. Tan, Y. Nishihata, J. Mizuki, K. Narita, M. Kimura and K. Kaneko, *Angew. Chemie*, 2006, **118**, 6144–6148.
- 40 H. Tanaka, M. Uenishi, M. Taniguchi, I. Tan, K. Narita, M. Kimura, K. Kaneko, Y. Nishihata and J. Mizuki, *Catal. Today*, 2006, **117**, 321–328.

View Article Online
DOI: 10.1039/D4TA03146F



- 41 V. B. Vert, F. V. Melo, L. Navarrete and J. M. Serra, *Appl. Catal. B Environ.*, [View Article Online
DOI: 10.1039/D4TA03146F](https://doi.org/10.1039/D4TA03146F) 2012, **115–116**, 346–356.
- 42 Y. Nishihata, J. Mizuki, T. Akao, H. Tanaka, M. Uenishi, M. Kimura, T. Okamoto and N. Hamada, *Nature*, 2002, **33**, 8–8.
- 43 V. Pérez-Dieste, L. Aballe, S. Ferrer, J. Nicolàs, C. Escudero, A. Milán and E. Pellegrin, *J. Phys. Conf. Ser.*, 2013, **425**, 072023.
- 44 S. Tanuma, C. J. Powell and D. R. Penn, *J. Electron Spectros. Relat. Phenomena*, 1990, **52**, 285–291.
- 45 C. J. Powell and A. Jablonski, *J. Surf. Anal.*, 2002, **9**, 322–325.
- 46 J. Moulder, W. Stickle, P. Sobol and K. Bomben, *Handbook of X-ray photoelectron spectroscopy*, 1992.
- 47 J. Wang, D. Kalaev, J. Yang, I. Waluyo, A. Hunt, J. T. Sadowski, H. L. Tuller and B. Yildiz, *J. Am. Chem. Soc.*, 2023, **145**, 1714–1727.
- 48 A. Nenning, A. K. Opitz, C. Rameshan, R. Rameshan, R. Blume, M. Hävecker, A. Knop-Gericke, G. Rupprechter, B. Klötzer and J. Fleig, *J. Phys. Chem. C*, 2016, **120**, 1461–1471.
- 49 O. Kwon, S. Joo, S. Choi, S. Sengodan and G. Kim, *J. Phys. Energy*, 2020, **2**, 032001.
- 50 O. Kwon, K. Kim, S. Joo, H. Y. Jeong, J. Shin, J. W. Han, S. Sengodan and G. Kim, *J. Mater. Chem. A*, 2018, **6**, 15947–15953.
- 51 T. Tan, Z. Wang, M. Qin, W. Zhong, J. Hu, C. Yang and M. Liu, *Adv. Funct. Mater.*, , DOI:10.1002/adfm.202202878.
- 52 Z. Du, H. Zhao, S. Yi, Q. Xia, Y. Gong, Y. Zhang, X. Cheng, Y. Li, L. Gu and K. Świerczek, *ACS Nano*, 2016, **10**, 8660–8669.
- 53 H. Lv, T. Liu, X. Zhang, Y. Song, H. Matsumoto, N. Ta, C. Zeng, G. Wang and X. Bao, *Angew. Chemie - Int. Ed.*, 2020, **59**, 15968–15973.
- 54 J. Wang, K. Syed, S. Ning, I. Waluyo, A. Hunt, E. J. Crumlin, A. K. Opitz, C. A. Ross, W. J. Bowman and B. Yildiz, *Adv. Funct. Mater.*, 2022, **32**, 1–15.



- 55 H. Summerer, A. Nenning, C. Rameshan and A. K. Opitz, *EES Catal.*, 2023, **1**, 274–289. View Article Online
DOI: 10.1039/D4TA03146F
- 56 J. Wang, J. Yang, A. K. Opitz, W. Bowman, R. Bliem, G. Dimitrakopoulos, A. Nenning, I. Waluyo, A. Hunt, J.-J. Gallet and B. Yildiz, *Chem. Mater.*, 2021, **33**, 5021–5034.
- 57 H. Lv, L. Lin, X. Zhang, R. Li, Y. Song, H. Matsumoto, N. Ta, C. Zeng, Q. Fu, G. Wang and X. Bao, *Nat. Commun.*, 2021, **12**, 5665.
- 58 A. J. Carrillo, A. H. Bork, T. Moser, E. Sediva, Z. D. Hood and J. L. M. Rupp, *Adv. Energy Mater.*, 2019, **9**, 1803886.
- 59 Q. H. Wu, M. Liu and W. Jaegermann, *Mater. Lett.*, 2005, **59**, 1480–1483.
- 60 P. A. Spevack and N. S. McIntyre, *J. Phys. Chem.*, 1992, **96**, 9029–9035.
- 61 E. J. Crumlin, E. Mutoro, W. T. Hong, M. D. Biegalski, H. M. Christen, Z. Liu, H. Bluhm and Y. Shao-Horn, *J. Phys. Chem. C*, 2013, **117**, 16087–16094.
- 62 B. Koo, K. Kim, J. K. Kim, H. Kwon, J. W. Han and W. C. Jung, *Joule*, 2018, **2**, 1476–1499.
- 63 C. Riedl, M. Siebenhofer, A. Nenning, A. Schmid, M. Weiss, C. Rameshan, A. Limbeck, M. Kubicek, A. K. Opitz and J. Fleig, *J. Mater. Chem. A*, 2022, **10**, 14838–14848.
- 64 I. Lucentini, X. Garcia, X. Vendrell and J. Llorca, *Ind. Eng. Chem. Res.*, 2021, **60**, 18560–18611.



Data availability

The authors confirm that the data supporting the findings of this study are available within the article and its ESI. All the experimental data will be available on request.

